MNRAS 000, 1–18 (2016) Preprint 10 March 2022 Compiled using MNRAS LATEX style file v3.0

Reconstruction of halo power spectrum from redshift-space galaxy distribution: cylinder-grouping method and halo exclusion effect

Teppei Okumura,[1,2⋆] Masahiro Takada,[1] Surhud More[1] and Shogo Masaki[3]

[1] *Kavli Institute for the Physics and Mathematics of the Universe (WPI), The University of Tokyo Institutes for Advanced Study, The University of Tokyo, Kashiwa, Chiba 277-8583, Japan*

[2] *Institute of Astronomy and Astrophysics, Academia Sinica, P. O. Box 23-141, Taipei 10617, Taiwan*

[3] *NTT Secure Platform Laboratories, NTT Corporation, Tokyo 180-8585, Japan*

arXiv:1611.04165v2 [astro-ph.CO] 18 Mar 2017

10 March 2022

ABSTRACT

The peculiar velocity field measured by redshift-space distortions (RSD) in galaxy surveys provides a unique probe of the growth of large-scale structure. However, systematic effects arise when including satellite galaxies in the clustering analysis. Since satellite galaxies tend to reside in massive halos with a greater halo bias, the inclusion boosts the clustering power. In addition, virial motions of the satellite galaxies cause a significant suppression of the clustering power due to nonlinear RSD effects. We develop a novel method to recover the redshift-space power spectrum of halos from the observed galaxy distribution by minimizing the contamination of satellite galaxies. The cylinder grouping method (CGM) we study effectively excludes satellite galaxies from a galaxy sample. However, we find that this technique produces apparent anisotropies in the reconstructed halo distribution over all the scales which mimic RSD. On small scales, the apparent anisotropic clustering is caused by exclusion of halos within the anisotropic cylinder used by the CGM. On large scales, the misidentification of different halos in the large-scale structures, aligned along the line-of-sight, into the same CGM group causes the apparent anisotropic clustering via their cross-correlation with the CGM halos. We construct an empirical model for the CGM halo power spectrum, which includes correction terms derived using the CGM window function at small scales as well as the linear matter power spectrum multiplied by a simple anisotropic function at large scales. We apply this model to a mock galaxy catalog at $z = 0.5$, designed to resemble SDSS-III BOSS CMASS galaxies, and find that our model can predict both the monopole and quadrupole power spectra of the host halos up to $k < 0.5\,h\,\mathrm{Mpc}^{-1}$ to within 5%.

Key words: cosmology: theory — cosmological parameters — dark energy — galaxies: halos — large-scale structure of universe — methods: statistical

1 INTRODUCTION

Observation of large-scale structure of the Universe through imaging and spectroscopic surveys of galaxies is a powerful tool to probe the origin of the accelerated expansion of the Universe, i.e., dark energy or its alternative such as modified gravity theories (e.g., see Weinberg et al. 2013, for a review). Imaging surveys enable us to probe the growth of cosmic structure through observations of the gravitational lensing effect. On the other hand, spectroscopic surveys provide information on the expansion rate through baryon acoustic oscillations (BAO). Due to the fact that the distance to each galaxy is measured by redshift, spectroscopic surveys also enable us to probe the growth rate of the structure by measuring redshift-space distortions (RSD) (Kaiser 1987; Hamilton 1998). Combining imaging and spectroscopic surveys is a powerful tool to study the origin of the cosmic acceleration.

While the BAO scale can be precisely predicted, the constraints from RSD are known to be affected by various systematic effects (e.g., Tinker et al. 2006; Okumura & Jing 2011; Jennings et al. 2011). One of the most serious systematic effects arises from the nontrivial relationship between dark matter halos and galaxies, especially due to the presence of "satellite" galaxies in the clustering analysis. Since satellite galaxies tend to reside in massive halos, which are more biased tracers and rare objects, the massive halos are upweighted in the clustering analysis, boosting the clustering amplitude compared to the bias of typical halos hosting other majority of the galaxies. In addition, virial motions of satellite galaxies inside such massive halos, known as the Finger-of-God (FoG) effect (Jackson 1972), cause a significant modification of the redshift-space clustering power at small scales. Thus, a direct approach of comparing the measured galaxy power spectrum with theory re-

⋆ tokumura@asiaa.sinica.edu.tw

© 2016 The Authors

quires a detailed knowledge of how galaxies populate their dark matter halos as a function of redshift, and perhaps their surrounding environments (Reid et al. 2014).

One way to connect theory and observations is an analytical approach based on cosmological perturbation theory (Bernardeau et al. 2002) and including an empirical FoG damping function (Peacock & Dodds 1994; Scoccimarro 2004; Okumura et al. 2012a; Zheng & Song 2016). While halos can be straightforwardly identified in N-body simulations (Davis et al. 1985; Behroozi et al. 2013), it is not straightforward to include halo bias prescriptions into the perturbation theory in a self-consistent manner, which generally requires many parameters to model halo bias at each order (e.g., Saito et al. 2014). Therefore, Okumura et al. (2015) proposed a hybrid method that combines perturbation theory or N-body simulations with a halo model to both model the galaxy clustering at large- and small-scales simultaneously (White 2001; Seljak 2001; Cooray & Sheth 2002; Mohammed & Seljak 2014; Seljak & Vlah 2015).

Another approach could be to modify the measurement method to correspond closely to theory. There are several clustering analysis methods in the literature which compress or filter out the impact of high-density galaxy regions (Tegmark et al. 2006; Simpson et al. 2013). Reid & Spergel (2009) used the redshift space friends-of-friends (FOF) percolation algorithm to group galaxies and demonstrated that the groups can be used to reconstruct the halo power spectrum from the distribution of luminous red galaxies (LRGs) in the Sloan Digital Sky Survey (SDSS) (Reid et al. 2010). If the halo power spectrum is recovered, we might not need to model the clustering signal from satellite galaxies and can directly compare the measured power spectrum with the theoretical predictions of halo clustering, based either on perturbation theory and/or N-body simulations (e.g., Matsubara 2008; Nishimichi & Taruya 2011; Sato & Matsubara 2011; Reid & White 2011; Okumura et al. 2012b; Nishizawa et al. 2013; Vlah et al. 2013). However, the accuracy of such a halo reconstruction method has not been fully assessed, and is known to strongly depend on the cylinder shape (or the linking length in redshift space) and the properties of the galaxy sample: the number density, the host halo mass and the satellite fraction. For example, since CMASS galaxy sample of the SDSS BOSS survey (Eisenstein et al. 2011) has a higher number density than that of LRGs by about factor of 3, a naive implementation of the FOF algorithm leads to a much deeper percolation of groups, and causes a large number of separate smaller halos to be grouped as one.

Hence the purpose of this paper is to revisit the halo reconstruction method proposed by Reid & Spergel (2009) and refine it to enable a more accurate recovery of the halo power spectrum. Instead of the FOF method, we adopt a similar but simpler cylinder grouping (CG) method. We then include terms to correct for the apparent anisotropic clustering caused by the anisotropic shape of our cylinder as well as by the large-scale clustering of halos misidentified by the CG method, extending the method in (van den Bosch et al. 2013; Baldauf et al. 2013). We will carefully investigate the accuracy and performance of the method using mock galaxy catalogs that are constructed from N-body simulations.

The structure of this paper is as follows. In Section 2 we first motivate the present work. In Section 3 we present our theoretical formalism to reconstruct the power spectrum of halos from the observed distribution of galaxies. Section 4 describes N-body simulations, the catalogs of halos and subhalos, and the mock galaxy catalogs which we use to test our method. In Section 5 we show the numerical results of the reconstructed halo power spectrum in redshift space. We present a brief summary of our conclusions in Section 6. In Appendix A-D we test how the accuracy of our formalism changes if properties of target galaxy sample and the cylinder size for the CG method are changed. Unless stated, throughout this paper we adopt the flat ΛCDM model with a matter density $\Omega_{\rm m0} = 0.265$, baryon density $\Omega_{\rm b0} = 0.0448$, the spectral index $n_s = 0.963$, the rms density fluctuation in a sphere of radius $8\,h^{-1}{\rm Mpc}$, $\sigma_8 = 0.80$, and the Hubble parameter $h = 0.71$, which is consistent with the WMAP cosmology (Komatsu et al. 2009).

2 MOTIVATION

We begin by highlighting the impact of satellite galaxies on the measured power spectrum in real and redshift space. In Fig. 1, the solid curves correspond to the linear power spectra in real space and redshift space computed using the publicly available, CAMB code (Lewis et al. 2000), where the amplitudes are normalized so as to reproduce the spectrum amplitude for halos or galaxies at large scales $k = [0.01, 0.05]\ h\ {\rm Mpc}^{-1}$. These power spectra were calculated using 32 realizations of mock catalogs of CMASS-like galaxies at $z = 0.5$, which we will describe in Section 4 below in detail. For the spectrum of host halos, we used halos in the mock catalog that host at least one galaxy. Note that the galaxy power spectra are from the exactly same catalog of host halos as used in the halo power spectra, and the fraction of satellite galaxies is about 10% in each realization. The satellite galaxies, albeit a small fraction, affect the power spectrum over all scales as we will describe below.

First, let us consider the real-space power spectrum, as illustrated in the left panel of Fig. 1. On large length scales, i.e., for small k, the galaxy power spectrum generally has a greater amplitude than the halo power spectrum. This can be interpreted as follows. Satellite galaxies tend to reside in more massive halos, and such massive halos generally have a larger halo bias with respect to the underlying matter distribution. Thus, when satellite galaxies are included in the power spectrum estimation, such massive halos are counted multiple times, causing a boost in the power spectrum amplitude.

On the other hand, the galaxy spectrum on small scales, i.e., $k \gtrsim 0.1h/{\rm Mpc}$, has a contribution arising from correlations between two galaxies, either central-satellite galaxies or satellite-satellite galaxies in the same halo, the so-called 1-halo term (Seljak 2000; Cooray & Sheth 2002). The correlations are preferentially from massive halos that can host multiple galaxies inside. The 1-halo term causes a boost in the power spectrum amplitude than the halo power spectrum. The 1-halo term has a complex scale dependence due to various effects such as nonlinear clustering, the exclusion effect and the nonlinear bias effects (Peebles 1980; Smith et al. 2007; van den Bosch et al. 2013; Nishizawa et al. 2013; Baldauf et al. 2013; Mohammed & Seljak 2014; Okumura et al. 2015; Baldauf et al. 2016). The amount of the amplitude boost is sensitive to the details of the 1-halo term (the satellite fraction, the radial profile of satellite galaxies in the host halos, and the mass distribution of halos hosting multiple galaxies). On the other hand, the halo power spectrum arises from correlations between different halos, the 2-halo term alone.

However, redshift space distortions (RSD) due to peculiar motions of galaxies modify the shape of galaxy power spectrum in a complicated way, as illustrated in the right panel of Fig. 1, where

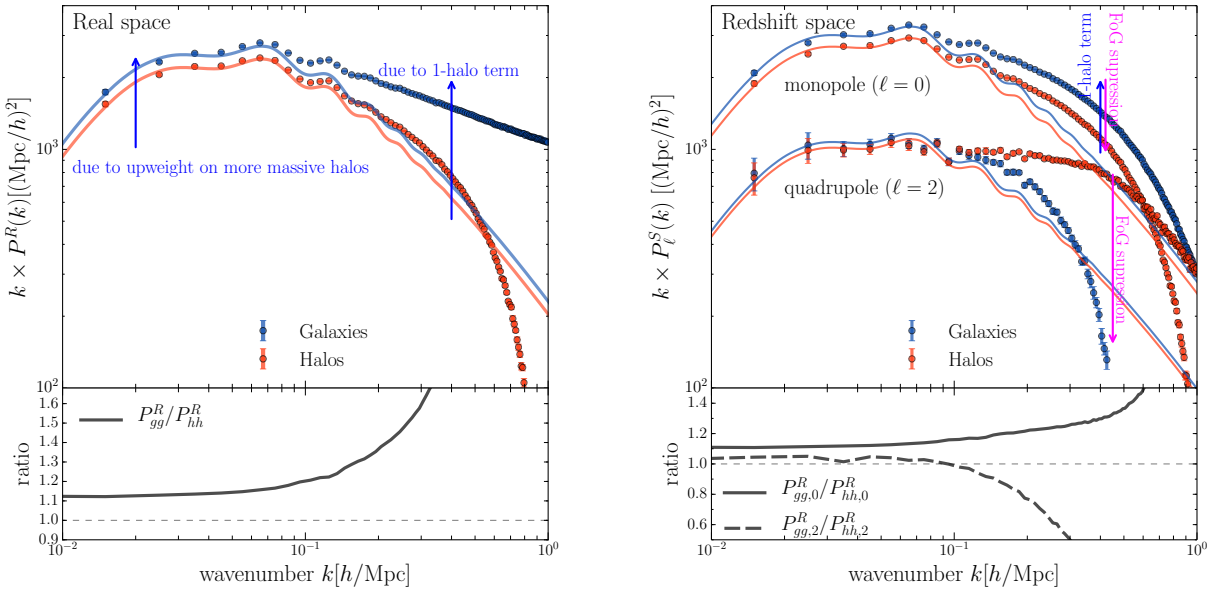


Figure 1. (*Top*) An illustration of how including satellite galaxies in the clustering analysis affects the real-space (left) and redshift-space (right) power spectrum, which are computed using the mock catalogs of CMASS-like galaxies and their host halos at $z = 0.5$. Errorbars are the standard error of the mean. The satellite galaxies alter the power spectrum amplitudes over all the scales, compared to the power spectrum of their host halos, due to the upweights on more massive halos with greater biases, the 1-halo term clustering contribution and the Finger-of-God effect in redshift space. These effects need to be properly taken into account in order to extract the information on the underlying matter power spectrum from the measured galaxy power spectrum if including satellite galaxies in the analysis. (*Bottom*) Ratios of the measured spectra of galaxies to those of their host halos. The deviation from unity is again caused by the satellite galaxies.

we show the monopole (P_0^S) and quadrupole (P_2^S) power spectra[1] (see equation 2 below for the definitions). The relative difference between the galaxy and halo power spectra at small k is similar to that in real space, although the difference in the quadrupole power spectrum is smaller due to the fact that it depends linearly on the galaxy bias (the monopole scales with bias as $P_0^S \propto b^2$ in the linear regime, while the quadrupole spectrum scales as $P_2^S \propto b$). At $k \gtrsim 0.1\ h$/Mpc, the virial motion of galaxies inside their host halos yields a significant suppression in the power for both the monopole and quadrupole power spectra, which is known as the Finger-of-God (FoG) effect (Jackson 1972). For the monopole spectrum, the FoG smearing effect somehow compensates the boost due to the 1-halo term contribution, making the overall shape closer to the halo power spectrum. This is, however, just a coincidence and the net power depends severely on the details of satellite galaxies in their host halos. For the quadrupole power spectrum, the FoG suppression leads to a much smaller amplitude in the power at $k \gtrsim 0.1\ h$/Mpc than that of the halo power spectrum.

Thus the difference between the power spectra of galaxies and their host halos at $k \gtrsim 0.1\ h$/Mpc seems to arise mainly from the satellite galaxies, which would prevent from recovering the underlying halo power spectrum. The purpose of this paper is to develop a method to reconstruct the halo power spectrum from the observed distribution of galaxies based on the CG halo reconstruction method.

[1] The superscript S denotes a quantity measured in redshift space.

3 FORMALISM

We decompose galaxies into two populations, central and satellite galaxies based upon their location in their host halos. Accordingly, as developed in Okumura et al. (2015) (also see Hikage et al. 2012; van den Bosch et al. 2013; Hikage et al. 2013), the galaxy power spectrum in redshift space can be decomposed into different contributions as

$$P^S_{\rm gg}(\mathbf{k}) = f_{\rm c}^2 P^S_{\rm cc}(\mathbf{k}) + 2 f_{\rm c} f_{\rm s} P^S_{\rm cs}(\mathbf{k}) + f_{\rm s}^2 P^S_{\rm ss}(\mathbf{k}), \quad (1)$$

where $P^S_{\rm cc}$, $P^S_{\rm ss}$ and $P^S_{\rm cs}$ are the auto power spectra of central and satellite galaxies, and their cross spectrum, respectively, $f_{\rm c}$ and $f_{\rm s}$ are the fractions of central and satellite galaxies to the total number of galaxies, respectively and satisfy $f_{\rm c} + f_{\rm s} = 1$, while $\mathbf{k}$ is the wavevector. We define the direction cosine of the angle between $\mathbf{k}$ and the line-of-sight direction as $\mu \equiv \hat{\mathbf{n}} \cdot \hat{\mathbf{k}}$, where $\hat{\mathbf{n}}$ is the unit vector along the line of sight. Note that, throughout this paper, we assume a distant observer approximation. The expression for the corresponding real-space power spectrum, denoted by the superscript R, can be obtained by taking the transverse modes; $P^R_{\rm gg}(k) = P^S_{\rm gg}(k, \mu = 0)$. Considering the multipole expansion in terms of the Legendre polynomials $\mathcal{L}_\ell(\mu)$ as

$$P^S_\ell(k) = \frac{2l+1}{2} \int_{-1}^{1} d\mu P^S(\mathbf{k}) \mathcal{L}_\ell(\mu), \quad (2)$$

we have

$$P^S_{{\rm gg},\ell}(k) = f_{\rm c}^2 P^S_{{\rm cc},\ell}(k) + 2 f_{\rm c} f_{\rm s} P^S_{{\rm cs},\ell}(k) + f_{\rm s}^2 P^S_{{\rm ss},\ell}(k). \quad (3)$$

Assuming statistical isotropy in the plane of the sky, the odd-number multipole spectra vanish. On the other hand, the statistical isotropy of the real-space power spectrum implies that only the monopole power spectrum is non-vanishing, i.e., $P^R_{{\rm gg},\ell}(k) = 0$ with $\ell \geqslant 2$.

In linear theory, the power spectrum for biased objects x(= g, c, etc.) can be described as (Kaiser 1987)

$$P^S_{\rm xx,lin}(\mathbf{k}) = (b_{\rm x} + f_{\rm g}\mu^2)^2 P^R_{\rm lin}(k), \quad (4)$$

where $b_{\rm x}$ is the linear bias parameter, $f_{\rm g}$ is the linear growth rate[2] defined as $f_{\rm g} = d\ln D/d\ln a$ and $P^R_{\rm lin}$ is the linear power spectrum of total matter in real space. By considering the multipole expansion (equation 2), only the lowest three moments (monopole, quadrupole and hexadecapole) have non-zero values in linear theory, and they can be written as (Hamilton 1992; Cole et al. 1994):

$$P^S_{\rm xx,0}(k) = \left(b_{\rm x}^2 + \frac{2}{3}b_{\rm x}f_{\rm g} + \frac{1}{5}f_{\rm g}^2\right) P^R_{\rm lin}(k), \quad (5)$$

$$P^S_{\rm xx,2}(k) = \left(\frac{4}{3}b_{\rm x}f_{\rm g} + \frac{4}{7}f_{\rm g}^2\right) P^R_{\rm lin}(k), \quad (6)$$

$$P^S_{\rm xx,4}(k) = \frac{8}{35}f_{\rm g}^2 P^R_{\rm lin}(k). \quad (7)$$

3.1 Cylinder grouping (CG) method for halo reconstruction

If central galaxies reside at the center and have the same velocity of the host halos, the power spectrum of central galaxies is equivalent to the halo power spectrum of host halos, $P^S_{\rm hh}$:

$$P^S_{\rm hh}(\mathbf{k}) = P^S_{\rm cc}(\mathbf{k}). \quad (8)$$

Thus, in such an ideal case, we can reconstruct the halo power spectrum from the catalog of central galaxies, which is a goal of this paper. However, in practice it is very difficult to identify central galaxies from observations. Therefore we need to consider the effects of possible contamination on the halo reconstruction.

In this paper, we use the "cylinder grouping method" (hereafter, CG or CGM) to minimize the satellite galaxy contamination. We implement this method as follows:

(i) Make a ranked list of galaxies in descending order of their luminosities or stellar masses.
(ii) Mark the top most galaxy in the ranked list as central and remove it from the list. Find any other galaxies within a cylinder around the central galaxy, defined by a base radius $\Delta r_\perp$, and height $\Delta r_\parallel$, respectively perpendicular and parallel to the line of sight, and mark them as satellite galaxies and remove them from the list as well.
(iii) Repeat step (ii) until the entire list is exhausted.

We hereafter refer to the galaxies marked as centrals as "CGM central galaxies" or "CGM halos", while we refer to the galaxies removed by the grouping method as "CGM satellite galaxies". We denote CGM central galaxies that do not have any satellite galaxy in their cylindrical region as "CGM isolated systems". On the other hand, we denote CGM central galaxies that have satellite galaxy(ies) in the cylinder region, as "CGM multiple systems".

Unless otherwise stated, we assume $\Delta r_\perp = 1.5\ h^{-1}\,{\rm Mpc}$ and $\Delta r_\parallel = 15\ h^{-1}\,{\rm Mpc}$ as our fiducial parameters for the size of the cylinder. A cylindrical shape is appropriate to group galaxies that are displaced along the line-of-sight due to RSD. The peculiar velocities of satellite galaxies within massive halos can displace them by up to $\sim$ a few $10\ h^{-1}\,{\rm Mpc}$. Hence $\Delta r_\parallel$ needs to be sufficiently large to cover a RSD effect due to virial motions of galaxies. in a massive halo.

[2] The linear growth rate $f_{\rm g}$ should not be confused with the fraction of an given sample x, $f_{\rm x}$, and should be distinguished.

Our method is based on a similar concept of the redshift space friends-of-friends method (Berlind et al. 2006), also used in the literature for the halo reconstruction (Reid & Spergel 2009; Hikage et al. 2013), but these methods are different in some of their technical and implementation aspects. An advantage of the cylinder grouping method compared to the redshift space friends-of-friends method is that the different CGM cylinders are not linked or connected. All the CGM central galaxies have exactly the same cylinder-shape territory region; no pair of the CGM central galaxies are closer in the separation than the cylinder size.

After removing CGM satellite galaxies, we *naively* expect that the power spectrum of the host halos can be reconstructed from the measured power spectrum of the central galaxies:

$$P^S_{\rm hh}(\mathbf{k}) \simeq \widetilde{P}^S_{\rm cc}(\mathbf{k}), \quad (9)$$

where tilde denotes a quantity for objects identified by the CG method, thus $\widetilde{P}^S_{\rm cc}$ is the power spectrum of the CGM central galaxies. Note that, it is plausible that some of the galaxies labeled centrals are in reality off-centered, so the power spectrum of central galaxies can differ from the halo power spectrum (Hikage et al. 2012, 2013). We will discuss this issue later in Appendix C.

Any method that groups observed galaxies together is subject to the following problems:

(i) *Group merging*: The CG method could mistakenly group together different halos into the same CGM halo.
(ii) *Group fragmentation*: The CG method could mistakenly fragment a single halo into different CGM halos.
(iii) *Central/satellite misidentification*: The CG method could mistake a central galaxy to be a satellite, and vice versa.

Of these, the first problem is quite significant, as the merging of groups, can preferentially happen in a high density region, or along a filament fortuitously oriented along the line-of-sight direction. This can result in an apparent *large scale anisotropy*, because correlations of the misidentified halos with other majority of CGM halos are removed from the clustering analysis. Furthermore the grouping method is not able to identify halos separated by the cylinder size, and thus suffer from a *cylindrical exclusion effect*. The anisotropic shape of the cylinder thus can introduce anisotropic effects in the measured power spectrum of the CGM halos. These anisotropic effects need to be corrected for before the measured power spectra of galaxies can be used to constrain cosmological parameters.

When central and satellite galaxies are identified based on the CG method, the decomposition equation of the power spectrum (equation 1) needs to be modified, as

$$P^S_{\rm gg}(\mathbf{k}) = \widetilde{f}_{\rm c}^2\widetilde{P}^S_{\rm cc}(\mathbf{k}) + 2\widetilde{f}_{\rm c}\widetilde{f}_{\rm s}\widetilde{P}^S_{\rm cs}(\mathbf{k}) + \widetilde{f}_{\rm s}^2\widetilde{P}^S_{\rm ss}(\mathbf{k}), \quad (10)$$

where $\widetilde{f}_{\rm c} + \widetilde{f}_{\rm s} = 1$. Note that this equation holds, independently of whether or not the CG method correctly identifies centrals and satellites.

3.2 Connecting the power spectrum of CGM halos to the halo power spectrum

Similarly to equation (10), one can write down the decomposition of the halo power spectrum based on the CG method, as

$$P^S_{\rm hh}(\mathbf{k}) = \widetilde{g}_{\rm c}^2\widetilde{P}^S_{\rm cc}(\mathbf{k}) + 2\widetilde{g}_{\rm c}\widetilde{g}_{\bar{\rm c}}\widetilde{P}^S_{\rm c\bar{c}}(\mathbf{k}) + \widetilde{g}_{\bar{\rm c}}^2\widetilde{P}^S_{\bar{\rm c}\bar{\rm c}}(\mathbf{k}) - 2\widetilde{g}_{\rm c}\widetilde{g}_{\bar{\rm s}}\widetilde{P}^S_{\rm c\bar{s}}(\mathbf{k}) - 2\widetilde{g}_{\bar{\rm c}}\widetilde{g}_{\bar{\rm s}}\widetilde{P}^S_{\bar{\rm c}\bar{\rm s}}(\mathbf{k}) + \widetilde{g}_{\bar{\rm s}}^2\widetilde{P}^S_{\bar{\rm s}\bar{\rm s}}(\mathbf{k}), \quad (11)$$

where the subscript $\bar{\rm c}$ denotes galaxies which are centrals but grouped together with another central(s) living in the more massive

halo(s) thus labeled as satellites, while galaxies with $\bar{\rm s}$ are satellites but failed to be identified by the CGM thus labeled as centrals. $\widetilde{g}_{\rm x}$ is similar to $\widetilde{f}_{\rm x}$ but the fraction to the total number of halos, $\widetilde{g}_{\rm x} = \widetilde{N}_{\rm x}/N_{\rm h} = \widetilde{N}_{\rm x}/N_{\rm c}$, thus $\widetilde{g}_{\rm c} + \widetilde{g}_{\bar{\rm c}} - \widetilde{g}_{\bar{\rm s}} = 1$. Note again that, with tilde, the subscript c denotes galaxies identified by the CGM as centrals, thus some of them are satellites in practice. Because $\widetilde{g}_{\rm c} \simeq 1 \gg \widetilde{g}_{\bar{\rm c}} > \widetilde{g}_{\bar{\rm s}}$ as we will see in Section 5.1, by keeping major terms, we have,

$$P^S_{\rm hh}(\mathbf{k}) \simeq \widetilde{P}^S_{\rm cc}(\mathbf{k}) + 2\left\{\widetilde{g}_{\bar{\rm c}}\widetilde{P}^{S1h}_{\rm c\bar{c}}(\mathbf{k}) - \widetilde{g}_{\bar{\rm s}}\widetilde{P}^{S1h}_{\rm c\bar{s}}(\mathbf{k})\right\} + 2\left\{\widetilde{g}_{\bar{\rm c}}\widetilde{P}^{S2h}_{\rm c\bar{c}}(\mathbf{k}) - \widetilde{g}_{\bar{\rm s}}\widetilde{P}^{S2h}_{\rm c\bar{s}}(\mathbf{k})\right\}, \quad (12)$$

where we explicitly write the contributions of $\widetilde{P}^S_{\rm c\bar{c}}$ at 1-halo and 2-halo regimes with the superscripts $1h$ and $2h$, respectively. The purpose of this paper is to reconstruct the halo power spectrum in redshift space, namely to model the total contributions from the terms of $\widetilde{P}_{\rm c\bar{c}}$ and $\widetilde{P}_{\rm c\bar{s}}$.

Instead of the naive reconstruction (equation 9), here we propose the following model to relate the power spectrum of CGM halos to that of underlying halos:

$$P^S_{\rm hh}(\mathbf{k}) \simeq \widetilde{P}^S_{\rm cc}(\mathbf{k}) + \left\{W(\mathbf{k}) + \left[W(\mathbf{k}) * \widetilde{P}^R_{\rm cc,0}(k)\right](\mathbf{k})\right\} + \Delta P^S(\mathbf{k}). \quad (13)$$

In the following we explain each term on the r.h.s. and how they intend to correct for the systematic effects described in the previous subsection.

The terms in the curly brackets arise from the Fourier transform of the correlation function with the exclusion effect (van den Bosch et al. 2013; Baldauf et al. 2013). They correspond to the contribution of the 1-halo terms in equation (12), and correct for the exclusion effect and the apparent anisotropy due to the cylinder shape, as discussed in the previous subsection. We extend the formalism in van den Bosch et al. (2013) and Baldauf et al. (2013) to account for a cylindrical window exclusion effect. The function $W(\mathbf{k})$ is the Fourier transform of the cylinder-shaped window, expressed as

$$W(\mathbf{k}) = 2\frac{J_1(k_\perp \Delta r_\perp)}{k_\perp \Delta r_\perp}\frac{\sin(k_\parallel \Delta r_\parallel)}{k_\parallel \Delta r_\parallel} V_W, \quad (14)$$

where V_W is the comoving volume of cylinder, $V_W = 2\pi(\Delta r_\perp)^2 \Delta r_\parallel$ (see § 5.2 for the shape of the window function). Note that the effective height of cylinder is $2 \times \Delta r_\parallel$ as centers of two CGM groups have to be separated by more than $\Delta r_\parallel$ for both positive and negative radial directions. The first term in the brackets corrects for the exclusion effect of CGM halo. The second term in the brackets primarily corrects for an apparent anisotropic clustering due to the convolution of the window function and the underlying halo power spectrum, assuming that the halo power spectrum is a smooth function at scales down to the virial radii of host halos, a few Mpc at maximum:

$$\left[W(\mathbf{k}) * \widetilde{P}^R_{\rm cc,0}(k)\right](\mathbf{k}) = \int \frac{{\rm d}^3\mathbf{q}}{(2\pi)^3} W(\mathbf{q})\widetilde{P}^R_{\rm cc,0}(|\mathbf{k}-\mathbf{q}|) = \int {\rm d}^3\mathbf{r}\, \mathcal{W}(\mathbf{r})\widetilde{\xi}^R_{\rm cc}(\mathbf{r}) e^{i\mathbf{k}\cdot\mathbf{r}}, \quad (15)$$

where $\mathcal{W}(\mathbf{r})$ is the cylinder window in real space.

The last term in equation (13) is intended to correct for an apparent anisotropic clustering due to the misidentified CGM halos. The misidentification of CGM halos occurs if central galaxies in different halos are grouped together by the CGM method and misidentified as satellite galaxies in the same CGM halo, or if satellite galaxies in the same halo are fragmented into different halos. These two cases correspond to $\widetilde{P}^{S2h}_{\rm c\bar{c}}$ and $\widetilde{P}^{S2h}_{\rm c\bar{s}}$ in equation (12), respectively. This misidentification preferentially occurs in an overdensity region in large-scale structure or if filamentary structure of large-scale structure is aligned to the line-of-sight direction. As a result, correlations of the misidentified halos in different overdensity regions with other majority of CGM halos are removed from the clustering analysis. Since this occurs in the 2-halo regime, we employ a minimal model to describe this effect; we assume that the contaminating effect is proportional to the linear power spectrum of total matter with an coefficient function including the distortion due the cylinders anisotropies, $\Delta P^S(\mathbf{k}) = \alpha(\mu) P^R_{\rm lin}(k)$. The linear power spectrum $P^R_{\rm lin}(k)$ can be computed using the public code such as CMBFAST (Seljak & Zaldarriaga 1996) or CAMB (Lewis et al. 2000) for a given cosmological model. If we apply this model in real space and adopt an isotropic group finder such as spheres rather than cylinders, the coefficient is just the square of the effective bias of the two 2-halo terms, $\alpha(\mu) = b^2_{\rm eff}$. The μ dependence is determined by both RSD and nature of misidentified halos. We will investigate the functional form of our model and its performance in detail in Section 5.

4 MOCK CATALOG OF REDSHIFT GALAXY SURVEY

In order to test the methodology developed in this paper and assess its performance, we use a mock catalog of galaxies that is constructed from N-body simulations for ΛCDM model. Here we describe the details of the construction of these catalogs.

4.1 N-body simulations and halo/subhalo catalogs

We use the 32 realizations of cosmological simulations presented by Sato & Matsubara (2011). Each realization evolves the matter density distribution as sampled by 1024^3 N-body particles in a box size of 1 h^{-1} Gpc. The adopted cosmological parameters are described in Section 1. We use the snapshots at redshifts $z = 0.5$ and 2 for each realization, to construct a mock catalog. We use the friends-of-friends (FoF) group finder (e.g., Davis et al. 1985) with a linking length of 0.2 in units of the mean interparticle spacing to create a catalog of halos from the simulation output and use the *SubFind* algorithm (Springel et al. 2001) to identify subhalos within each halo. In this paper, we use halos and subhalos with equal to or more than 20 particles. Each particle in a halo region is assigned either to a smooth component of the parent halo or to a satellite subhalo, where the smooth component contains the majority of N-body particles in the halo region. Hereafter we call the smooth component a central subhalo and call the subhalo(s) satellite subhalo(s). For each subhalo, we estimate its mass by counting the bounded particles, which we call the subhalo mass ($M_{\rm sub}$). We store the position and velocity data of particles in halos and subhalos at different redshifts. To estimate the virial mass ($M_{\rm halo}$) for each parent halo, we apply the spherical overdensity method to the FoF halo, where the spherical boundary region is determined by the interior virial overdensity, $\Delta_{\rm vir}$, relative to the mean mass density (Bryan & Norman 1998). The overdensity $\Delta_{\rm vir} \simeq 242$ at $z = 0.5$ for the assumed cosmological model.

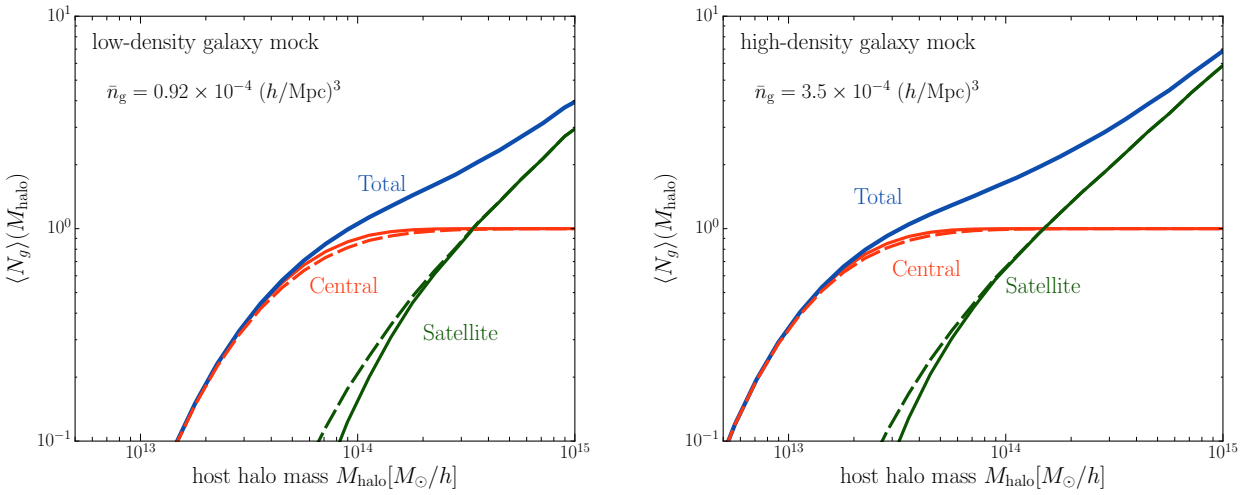


Figure 2. The halo occupation distribution (HOD) for galaxies in the mock catalog, constructed from N-body simulations (see text for details). The left and right panels show the HODs for the "low-density" and "high-density" galaxy mock catalogs that we will use in this paper. The upper bold solid curve in each panel is the total HOD, while the thin solid curves are the HODs for the central and satellite galaxies. Note that, if only a single galaxy of interest resides in the host halo, we refer to the galaxy as "central galaxy" in this paper, even if the galaxy resides in a satellite subhalo in the parent halo. The dashed curves show the HODs, if we count the off-centered galaxy as a satellite galaxy.

4.2 Abundance matching method in Masaki et al. (2013): populating galaxies into subhalos

To populate mock galaxies into halos in the simulation realization, we employ the abundance matching method described in Masaki et al. (2013). In brief, the method assumes that simulated halos at $z = 2$ are progenitors for early-type galaxies at low redshift, for which we adopt $z = 0.5$ in this paper. We label the most tightly bound particles in each progenitor halo as "star particles" as a building block of the early-type galaxy. We then label "galaxies" at the target low redshift, by identifying the subhalos containing a majority of the star particles in descending order of masses of the progenitor halos until the comoving number density of the matched subhalos becomes comparable to a target number density for the type of galaxies we may be interested in (see Masaki et al. 2013, for details). Note that building blocks ("star particles") in the different progenitor halos can merge together in the same subhalo at the low redshift. Thus the only free parameter in this method is the number density of progenitor halos at $z = 2$. In order to somewhat take into account stochastic nature of galaxy formation, we employ a similar model to the halo occupation distribution (HOD) (Cooray & Sheth 2002; Zheng et al. 2005) including a scatter around the halo mass threshold:

$$p(M; z = 2) = \frac{1}{2}\left[1 + \mathrm{erf}\left(\frac{\ln M - \ln M_{\rm th}}{\sqrt{2}\sigma}\right)\right], \qquad (16)$$

where $M_{\rm th}$ is a parameter to model the mass threshold for halo selection, and we fix the value of $\sigma = 0.5$. Note that, $p(M) = 0$ at $M \ll M_{\rm th}$, while $p(M) = 1$ at $M \gg M_{\rm th}$. According to the above probability in each mass bin, we randomly select progenitor halos in each mass bin from the halo catalog of a given simulation realization. The mass threshold parameter $M_{\rm th}$ is determined so that the resulting mock galaxy sample has a desired number density. In this paper, we consider two mock catalogs that differ in the target number density: $\bar{n}_g \simeq 3.4 \times 10^{-4}$ or 9.2×10^{-5} $(h\,\mathrm{Mpc}^{-1})^3$ which we will refer to as the "high-density" or "low-density" galaxy sample, respectively. The mass threshold parameter for these samples are $M_{\rm th} \simeq 3.1 \times 10^{12}\ h^{-1}M_\odot$ and $7.7 \times 10^{12}\ h^{-1}M_\odot$, respectively. We employed the fixed value of $M_{\rm th}$ for different realizations for simplicity, since the resulting number density of galaxies in different realizations is different only by less than 1%. The number density of the high-density galaxy mock is comparable with that for CMASS galaxies in the BOSS survey (Eisenstein et al. 2011), while the low-density sample is comparable with the number density for the LRG galaxies (Eisenstein et al. 2005; Reid & Spergel 2009) or the CMASS galaxy subsample with higher stellar mass threshold (e.g., More et al. 2015).

The main purpose of this paper is not to develop a sophisticated mock catalog of galaxies to reproduce observed properties of galaxies in any survey, but rather to use such a mock catalog to test the validity and performance of the halo reconstruction method. In this regard there are several advantages of this method. First, the mock catalog naturally consists of both central and satellite galaxies, rather than assuming the two populations as done in the HOD method. Secondly, each galaxy has its own peculiar motion, including both virial motion inside the host halo and the bulk motion of its host halo (the motion of central galaxy might be different from the center-of-mass motion of N-body particles in the host halo as studied in Masaki et al. 2013). Thirdly, this mock generally predicts that some fraction of halos do not host a central galaxy in its central subhalo, that is the off-centering effect. This also means that, even if a given halo hosts a single galaxy inside, the galaxy might be off-centered, or equivalently reside in a satellite subhalo (see Hikage et al. 2012; Masaki et al. 2013, for the similar discussion).

4.3 HOD and clustering properties of mock galaxies

Now we discuss properties of the mock galaxies in the context of large-scale structure. The left and right hand panels of Fig. 2 show the HOD for the galaxies in the "high-density" and "low-density" mock catalogs, respectively. Here we show the averaged HODs of the 32 realizations. The method we used allows us to compute the HODs directly from the mock catalog rather than assuming a particular functional form. The figure shows the central and satellite HODs. In our default definition, if a halo hosts a single galaxy

Mock galaxy catalogs

Mock	$\bar{n}_{\rm g}$ $[10^{-4}(\,h\,{\rm Mpc}^{-1})^3]$	$N_{\rm g}$	$f_{\rm sat}^{\rm gal}$ [%]	single system [%]	multiple systems [%] 2	3	4	5	6	$\geqslant 7$
high-dens	3.4	344, 296	9.59	91.75	6.64	1.14	0.30	0.10	0.04	0.03
low-dens	0.92	92, 362	7.27	93.44	5.59	0.76	0.16	0.04	0.01	0.006

Table 1. Details of mock galaxy catalogs, the "high-density" or "low-density" mock catalogs we use in this paper (see text for details). $\bar{n}_{\rm g}$ is the mean number density of galaxies, $N_{\rm gal}$ is the total number of galaxies in the simulation volume, $V = 1\ (\,h^{-1}\ {\rm Gpc})^3$, and $f_{\rm sat}^{\rm gal}$ is the fraction of satellite galaxies. The single system is the halo hosting a single galaxy inside, and the multiple systems are the halos hosting multiple galaxies. The numbers for these systems are the fraction of each system among all the host halos. All the numbers are the average values from the 32 realizations of the mock catalogs.

inside and even if the galaxy resides in a satellite subhalo of the host halo, we include the galaxy in the central HOD. For comparison we also show, by the dashed curve, the central HOD obtained only by counting the galaxies residing in the central subhalos. The HOD for the high-density galaxy mock extends to lower halo mass. Qualitatively speaking the shapes of the HODs for our mock catalog appear to be similar to those for the CMASS and LRG galaxies (White et al. 2011; More et al. 2015).

Table 1 summarizes the properties of the mock galaxy catalogs. The fractions of satellite galaxies to all the galaxies are about 9.6% and 7.3% for the high- and low-density galaxy mocks, respectively. The table also shows fractions of "single" or "multiple" halo systems among all the host halos where the single systems are the halos hosting a single galaxy inside and the multipole systems are the halos hosting multiples galaxies.

Next we discuss clustering properties of these mock galaxies. We measure power spectra of given galaxy samples using a standard fast Fourier transform (FFT) method, following the previous work of Okumura et al. (2012a,b, 2015). We first define the density field by using a grid of 1024^3 cells with cloud-in-cell interpolation. When measuring the redshift-space density field, the positions of objects are displaced along the line-of-sight direction according to their peculiar velocities before they are assigned to the grid. We then perform an FFT to convert the density field of sample "x" to Fourier space, $\delta_{\rm x}(\mathbf{k})$. The power spectrum $P_{\rm xx}^S(\mathbf{k})$ is obtained by averaging $|\delta_{\rm x}^2(\mathbf{k})|$ over finite bins in $\mathbf{k}$. We assume the shot noise to be Poisson, and hence subtract $1/\bar{n}_{\rm x}$ from the measured auto power spectrum. In case of the cross power spectrum of samples "x" and "y", $P_{\rm xy}^S(\mathbf{k})$, the two fields need to be multiplied. The aliasing effect arising from the cloud-in-cell mass assignment method is corrected for using the formula of Jing (2005). The errorbars are estimated from the standard deviation of the 32 realizations, and the scatter is divided by the square root of the number of the realizations, i.e., $\sqrt{32}$, to show the error of the mean.

Fig. 1 shows the real- and redshift-space power spectra for the "low-density" galaxy mock. Even if the fraction of satellite galaxies is only 7% (see Table 1), the galaxies cause a large difference from the underlying halo power spectra, as discussed in Sec. 2 in detail.

The projected correlation function can be obtained by projecting the redshift-space correlation function along the radial direction:

$$w_p(r_p) = \int_{-r_{\parallel,\rm max}}^{r_{\parallel,\rm max}} {\rm d}r_\parallel \xi^s(r_\perp, r_\parallel), \tag{17}$$

where we choose $r_{\parallel,\rm max} = 100\ \ h^{-1}\ {\rm Mpc}$. In Fig. 3 we show the projected correlation functions measured from our mock samples. Roughly speaking, the projected correlation functions measured from the low- and high-density mocks are similar to the SDSS CMASS measurements in More et al. (2015).

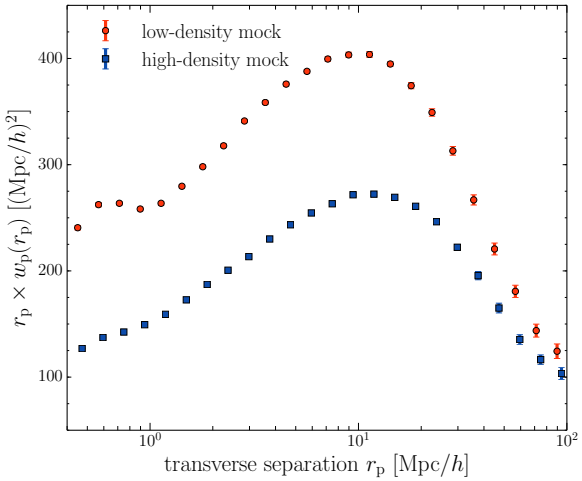


Figure 3. Projected correlation function, $r_p \times w_p(r_p)$, measured from the mock catalogs. The errorbars are the rms of the mean estimated from the 32 realizations each of which has volume of $1\ (\,h^{-1}\ {\rm Gpc})^3$.

5 NUMERICAL ANALYSIS

In this section we show the main results of this paper, i.e. the reconstruction of the halo distribution and power spectra from the galaxy distribution using the mock catalogs.

5.1 Applying the CGM halo reconstruction to mock galaxy catalogs

In order to perform the CGM halo reconstruction, we need to specify the parameters that characterize the cylinder around each galaxy, the height ($\Delta r_\parallel$) and the base-circle radius ($\Delta r_\perp$), which are defined parallel and perpendicular to the line of sight, respectively. They are arbitrary and need to be chosen so that galaxies which are in the same halo are properly grouped into the same CGM halo. In particular, the value of $\Delta r_\parallel$ needs to be carefully tuned because the inferred radial separation between galaxies is affected by their peculiar velocities due to virial motions, i.e the FoG effect. For the LRG sample at $z \sim 0.3$, which has a number density of $10^{-4}\ (\,h\,{\rm Mpc}^{-1})^3$, Reid & Spergel (2009) adopted

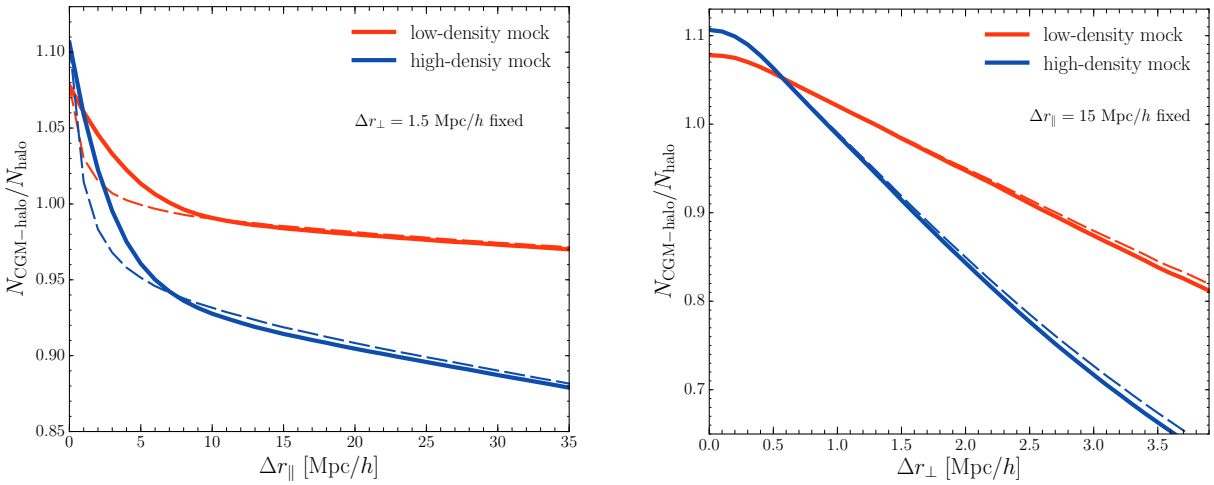


Figure 4. The number of halos identified using the cylinder-grouping method (CGM) relative to the true number. The left panel shows the result as a function of the height of the cylinder, $\Delta r_\parallel$, with its base circle radius being fixed to $\Delta r_\perp = 1.5\,h^{-1}$ Mpc, while the right panel as a function of $\Delta r_\perp$ with the height being fixed to $\Delta r_\parallel = 15\,h^{-1}$ Mpc. The red and blue lines are for the low- and high-density mocks, respectively. The dashed lines are obtained when the cylinders are identified in real space, while the solid lines are when identified in redshift space.

CGM halo catalogs

Mock	$N_{\rm h}$	cylinder identification	$\tilde{N}_{\rm h}$	$\tilde{f}_{\rm sat}^{\rm gal}$ [%]	single system [%]	multiple systems [%] 2	3	4	5	6	$\geqslant 7$
high-dens	311,277	real space	286,080 (91.9%)	16.91	84.06	12.65	2.48	0.58	0.16	0.04	0.02
		redshift space	284,681 (91.5%)	17.32	83.67	12.90	2.59	0.61	0.16	0.05	0.02
low-dens	85,661	real space	84,394 (98.5%)	8.63	91.74	7.27	0.85	0.12	0.02	0.005	0.001
		redshift space	84,257 (98.4%)	8.77	91.58	7.41	0.87	0.12	0.02	0.004	0.001

Table 2. Details of CGM halos for the low- and high-density mock catalogs, compared to Table 1. Here the CGM-halos are the halos reconstructed by placing the cylinder around each of more massive galaxies and by then removing satellite galaxies within a cylinder around the central galaxy. (see text for the details). We employed $\Delta r_\perp = 1.5\ h^{-1}$ Mpc and $\Delta r_\parallel = 15\ h^{-1}$ Mpc for the radius and height of the CGM cylinder, and included the redshift space distortion of galaxies when implementing the CGM method in redshift space. The single CGM-halos are the isolated systems, and the multipole CGM-halos are the systems containing satellite galaxies in the same CGM halo. The satellite fraction $\tilde{f}_{\rm sat}^{\rm gal}$ is the fraction of the CGM satellite galaxies among all the galaxies.

$(\Delta r_\perp, \Delta r_\parallel) = (0.8, 20)[\,h^{-1}\,{\rm Mpc}]$ to implement their halo reconstruction.

In this paper we adopt $(\Delta r_\perp, \Delta r_\parallel) = (1.5, 15)[\,h^{-1}\,{\rm Mpc}]$ as our default parameters. The left panel of Fig. 4 shows the ratio of the number of halos identified by the CG technique to the true number of halos as a function of $\Delta r_\parallel$, for a fixed value of $\Delta r_\perp = 1.5\,h^{-1}$ Mpc. The red line corresponds to the low-density mock galaxy sample (see Table 1), while the blue line corresponds to the high-density mock sample. In the ideal case where equation (8) holds, this ratio becomes unity, which requires a fine tuning of the parameters, $(\Delta r_\perp, \Delta r_\parallel)$. However, an *apparent* perfect reconstruction, i.e. the ratio being unity, could happen by chance, if the CGM halos contain both misidentified halos (identifying satellite galaxies as different halos) and different halos mis-grouped and identified as one halo. Thus the perfect reconstruction cannot be realized in practice.

The solid and dashed curves show the results for the cases where cylinders are identified by the positions of galaxies in redshift and real space, respectively. The discrepancy between the two results seen at small $\Delta r_\parallel$ for both high and low density samples implies that the length of the cylinder is not long enough to capture the line-of-sight shifts of the galaxies due to RSD. The right panel of Fig. 4 is the same as the left panel but shows the ratios as a function of $\Delta r_\perp$, fixing $\Delta r_\parallel = 15\,h^{-1}$ Mpc. Since the angular positions are not affected by RSD, the results where cylinders are defined in real space and redshift space are almost the same, and the number of the CGM halos decreases linearly with $\Delta r_\perp$. For the low-density mock catalog which has the number density $\bar{n}_{\rm g} \simeq 10^{-4}\ (\,h\,{\rm Mpc}^{-1})^3$, similar to that of LRGs, the choices of $\Delta r_\perp = 1.5\ h^{-1}$ Mpc and $\Delta r_\parallel = 15\ h^{-1}$ Mpc seem reasonable. For the high-density mock, the smaller size cylinder seems better, but we in this paper employ the same parameters for simplicity. In Appendix A, we will show how the size of the cylinder affects the final results, by adopting $\Delta r_\parallel = 30\,h^{-1}$ Mpc.

Table 2 gives a summary of the halo catalogs reconstructed from the CG method using the fiducial parameters $(\Delta r_\perp, \Delta r_\parallel) = (1.5, 15)\ h^{-1}$ Mpc. The number of the CGM halos is smaller than that of the underlying true halos, because the CG method incorrectly connects different halos. For the high-density mock, this problem is worse. Compared to Table 1, the fractions of the single or multiple systems, which contain single or multiple galaxies in the CGM halos, respectively, are modified. These are unavoidable limitations of the CG method, and below we will carefully study the impact of these effects on the reconstructed halo power spectra. For the low- and high-density mocks, $(\widetilde{g}_{\rm c}, \widetilde{g}_{\bar{\rm c}}, \widetilde{g}_{\bar{\rm s}}) = (0.985, 0.0335, 0.0187)$ and

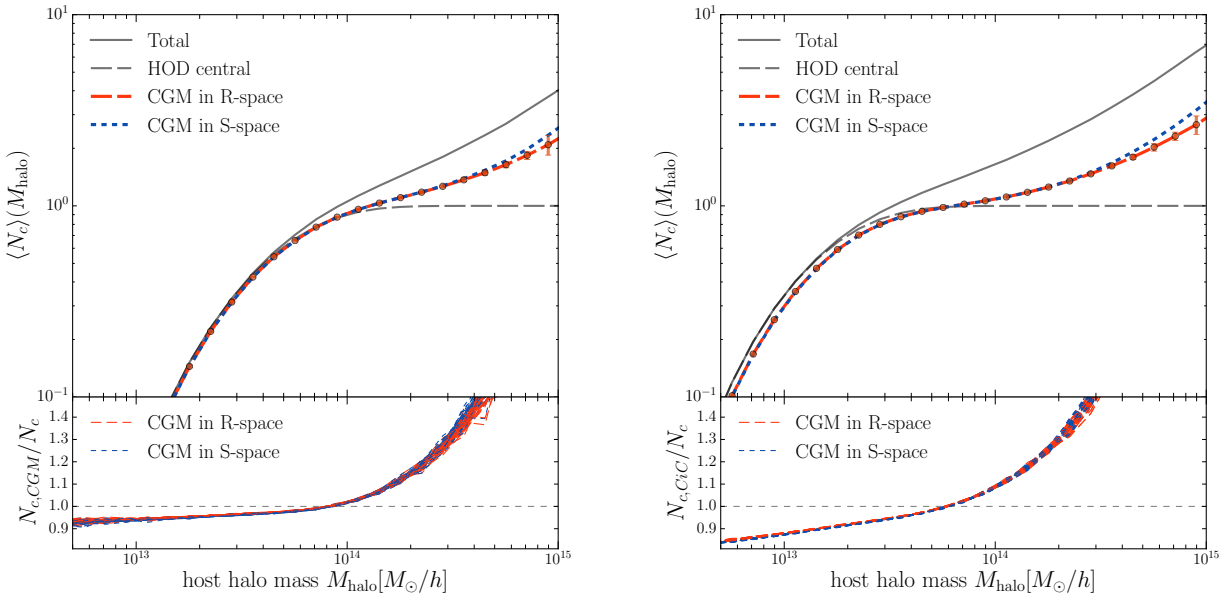


Figure 5. (*Top*) The HOD for central galaxies identified by the CG method for the low- and high-density mock catalogs in the left and right panels, respectively. The red-dashed curves are obtained when the cylinders are identified in real space, while the blue-dotted curves are when identified in redshift space. The central HOD becomes larger than unity for massive halos because multiple galaxies in a massive halo can be misidentified as different CGM halos. The gray solid and dashed curves are the total and central HOD which are the same as the blue and red solid curves in Fig. 2, respectively. (*Bottom*) The ratio of the CGM central galaxies to the true central galaxies. The ratio being less than unity for low-mass halos means that the galaxies in different halos are mis-grouped into one halo.

$(0.919, 0.0951, 0.0141)$, respectively, thus equation (12) is a good approximation especially for our main, low-density sample.

The top left panel of Fig. 5 shows the HOD for central galaxies with lower density identified by the CG method. The red-dashed curve is obtained when the cylinders are identified in real space, while the blue-dotted curve is when identified in redshift space. The central HOD becomes larger than unity at the host halo mass of $M_{\rm halo} > 10^{14}(h^{-1}M_\odot)$. This is mainly caused by misidentification of different (central and satellite) galaxies in massive halos as different CGM halos, that are separated along the transverse direction to the light of sight direction rather than the radial direction. We confirmed this; if we change the radius of cylinder base circle to $\Delta r_\perp = 3\ h^{-1}\,{\rm Mpc}$ from the fiducial value $\Delta r_\perp = 1.5\ h^{-1}\,{\rm Mpc}$, the central HOD becomes below unity up to more massive halos. In other words, the CG method properly removes satellite galaxies along the radial direction that are a dominant source of the FoG effect. One can thus see such a misidentification is a minor effect which occurs only in the rare, massive halos. The gray solid and dashed curves are the same as the blue and red solid curves at the left panel of Fig. 2, respectively, and shown here for comparison. The bottom left panel of Fig. 5 shows the ratio of the central galaxies identified by the CGM to the true central galaxies. The ratio being less than unity for low-mass halos with $M_{\rm halo} < 10^{14}(h^{-1}M_\odot)$ means that the galaxies in different halos are mis-grouped into one halo. This is the dominant effect which we will try to correct for in the following subsections. The right panel of Fig. 5 is the same as the left panel but for the CGM central galaxies for the high-density mock. The fact that the deviation from unity at low $M_{\rm halo}$ at the bottom panel than that in the low density sample implies that the larger correction is required to reconstruct the halo spectrum for the higher density sample.

To conclude, the CGM single and multiple halo systems are different from the underlying true systems of halos given in Table 1, due to the imperfect grouping by the CG method. Some CGM central galaxies are satellite galaxies in larger more massive halos. Similarly, some CGM satellite galaxies are in reality central galaxies, either due to group misidentification, or a central-satellite misclassification.

5.2 Decomposed power spectra of CGM galaxies

As we have described, the CG halo reconstruction method has its limitations, which makes it difficult to obtain a perfect reconstruction of the underlying halos that host galaxies of interest. To better understand the halo reconstruction obtained by the CG method, in this subsection we consider the power spectrum decomposed into different correlation contributions between the central and satellite galaxies in the CGM halos, as given in equation (3). In the following we focus only on the low-density mock catalog.

In the left panel of Fig. 6, we first study the monopole power spectra of the galaxies in real space. The circle symbols are the monopole spectrum for all the galaxies in the mock catalog, the same spectrum shown in the left panel of Fig. 1. The bold red and yellow curves are respectively the spectra of the CGM "central" and "satellite" galaxies, while the bold green curve is their cross spectrum. Again note that the CGM satellites contain misidentified halos as we have discussed. The power spectrum of the galaxies is given by the sum of the central and satellite power spectra, weighted by their fractions (see equation 3). The power spectrum of the CGM central galaxies has lower amplitudes at large and small scales (small and large k bins) than the galaxy power spectrum. This is because more massive halos are weighted low and the 1-halo term contribution is mitigated. However, the power spectrum of CGM halos still does not correspond to that of the underlying halos.

In the right panel of Fig. 6 we show the anisotropic compo-

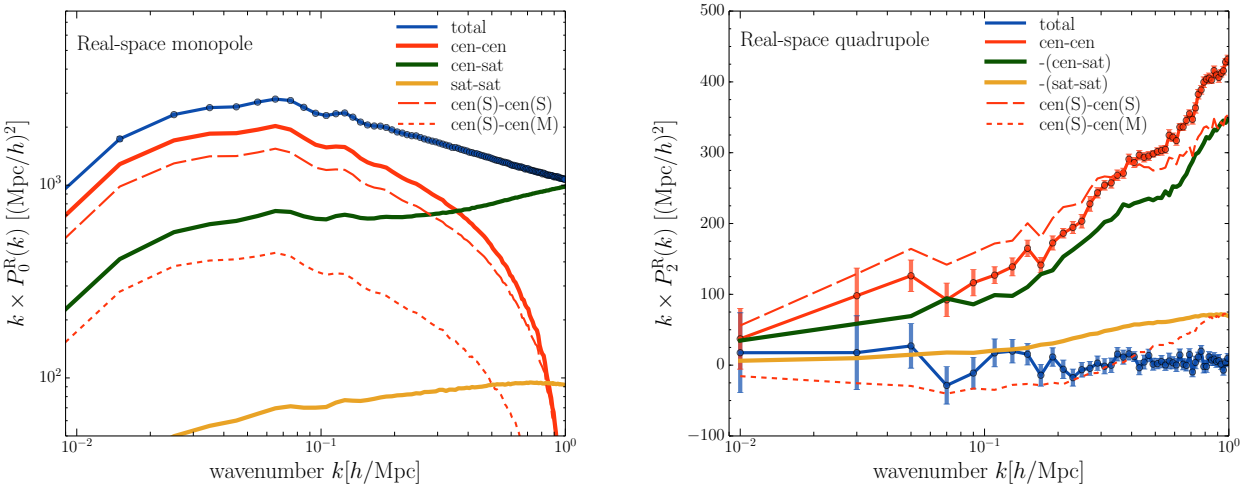


Figure 6. *Left panel*: Contributions of the decomposed galaxy samples by the CG method to the monopole power spectrum of the whole galaxies in real space. The red and yellow solid curves are the contribution from the central galaxies and satellite galaxies, denoted as $\widetilde{P}^R_{\rm cc,0}$ and $\widetilde{P}^R_{\rm ss,0}$, respectively, while the green curve is from their cross-spectrum $\widetilde{P}^R_{\rm cs,0}$. The power of $\widetilde{P}_{\rm cc,0}$ is further decomposed to the three, and two of them are displayed; the long- and short-dashed curves show the correlation of the centrals in the single systems, denoted as cen(S)-cen(S), and the cross-correlation of centrals in the single system and multiple system, cen(S)-cen(M), respectively. For illustrative purpose, the errorbars are shown only for the total power spectrum $P_{\rm gg,0}$. *Right*: The similar to the left panel, but for the quadrupole spectrum. Note that the total power is equal to a null signal as shown by the blue curve because of the cosmological principle. Thus the errorbars are added here to the main component, the quadrupole of the central galaxies $\widetilde{P}^R_{\rm cc,2}$. Note that $\widetilde{P}^R_{\rm cs,2}$ and $\widetilde{P}^R_{\rm ss,2}$ are multiplied by (-1).

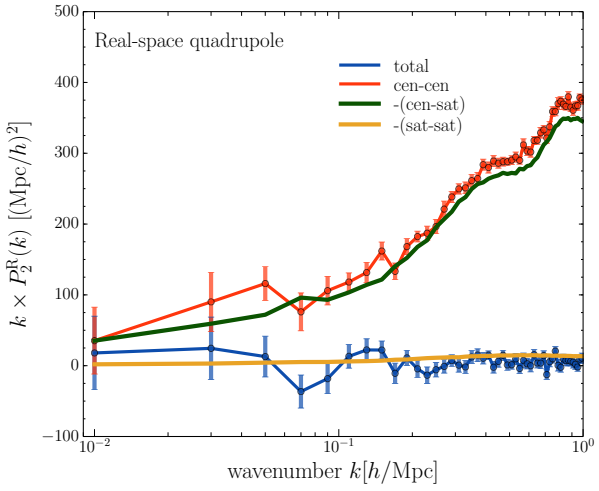


Figure 7. Same as the right panel of Fig. 6 but the CGM technique applied to the halo catalog.

nent, the quadrupole spectrum in real space. The quadrupole of the whole galaxy sample is equal to zero because the real-space galaxy distribution is isotropic, as shown with the blue points. The real-space power spectrum of the CGM central galaxies, however, has a non-zero quadrupole as shown by the red solid curve with the errorbars. Because the total power $P^R_{\rm gg,2} = 0$, the sum of the other two power spectra, the cross power spectrum of the CGM halos and satellites and the auto spectrum of the satellites, has the same amplitude as the power of the CGM central galaxies but the opposite sign. The dashed curve shows that the apparent quadrupole power arises mainly from the correlation between central galaxies in single CGM halos. The contribution from the $P^R_{\rm ss}$ is negligibly small because the amplitude is suppressed by the square of satellite galaxy fraction, $\widetilde{f}_{\rm s}^2$, where $\widetilde{f}_{\rm s} \sim 0.1$ for our mock galaxy catalog, thus $\widetilde{f}_{\rm c}\widetilde{P}^R_{\rm cc,2} \simeq -2\widetilde{f}_{\rm s}\widetilde{P}^R_{\rm cs,2}$. In particular, since the CGM satellites include misidentified halos in the overdensity region, the apparent quadrupole power at large scales can be understood to arise from cross-correlations of the misidentified halos with other majority of the central CGM galaxies. We also measured the multipoles of the decomposed galaxies in redshift space. The trend of each spectrum is more or less the same as shown in Fig. 5 of Okumura et al. (2015), thus we do not show the redshift-space spectra of the decomposed CGM galaxies in this paper and we refer readers to Okumura et al. (2015).

In order to see if the large-scale quadrupole is really caused by the misidentified halos, we consider to apply the CG method to the host halo distribution. In this case there is no satellite galaxy misidentified as a halo center ($\widetilde{g}_{\bar{\rm h}\bar{\rm h}} = 0$), so the equation (11) is simplified as,

$$\begin{aligned} P^S_{\rm hh}(\mathbf{k}) &= \widetilde{g}^2_{\rm h}\widetilde{P}^S_{\rm hh}(\mathbf{k}) + 2\widetilde{g}_{\rm h}\widetilde{g}_{\bar{\rm h}}\widetilde{P}^S_{\rm h\bar{h}}(\mathbf{k}) + \widetilde{g}^2_{\bar{\rm h}}\widetilde{P}^S_{\bar{\rm h}\bar{\rm h}}(\mathbf{k}) \\ &\simeq \widetilde{P}^S_{\rm hh}(\mathbf{k}) + 2\widetilde{g}_{\bar{\rm h}}\widetilde{P}^S_{\rm h\bar{h}}(\mathbf{k}), \end{aligned} \tag{18}$$

where $\widetilde{g}_{\rm h} = 1 - \widetilde{g}_{\bar{\rm h}} = 0.967$ when we adopt the same cylinder size, $(\Delta r_\perp, \Delta r_\parallel) = (1.5, 15)\, h^{-1}$ Mpc, for the host halos of the low-density sample. We measure the real-space quadrupole spectra of the halos and show them in Fig. 7. The contributions of $\widetilde{P}^S_{\rm hh}$, $\widetilde{P}^S_{\rm h\bar{h}}$ and $\widetilde{P}^S_{\bar{\rm h}\bar{\rm h}}$ to the total quadrupole are shown as the red, green and yellow lines, respectively. The contribution of $\widetilde{P}^S_{\bar{\rm h}\bar{\rm h}}$ is suppressed by $\widetilde{g}^2_{\bar{\rm h}} \sim 10^{-4}$ and negligibly small, as expected, thus $\widetilde{P}^S_{\rm hh,2} \simeq -2\widetilde{g}_{\bar{\rm h}}\widetilde{P}^S_{\rm h\bar{h},2}$ because the real-space quadrupole of halos is zero. Even for this case where there is no satellite, one can see a clear non-zero signal of the quadrupole at small-k, whose amplitude is similar to the quadrupole of the CGM halos identified from the galaxies as shown in the right panel of Fig. 6. This confirms that the large-scale anisotropy is indeed due to the central galaxies misidentified as satellite galaxies.

[bt]

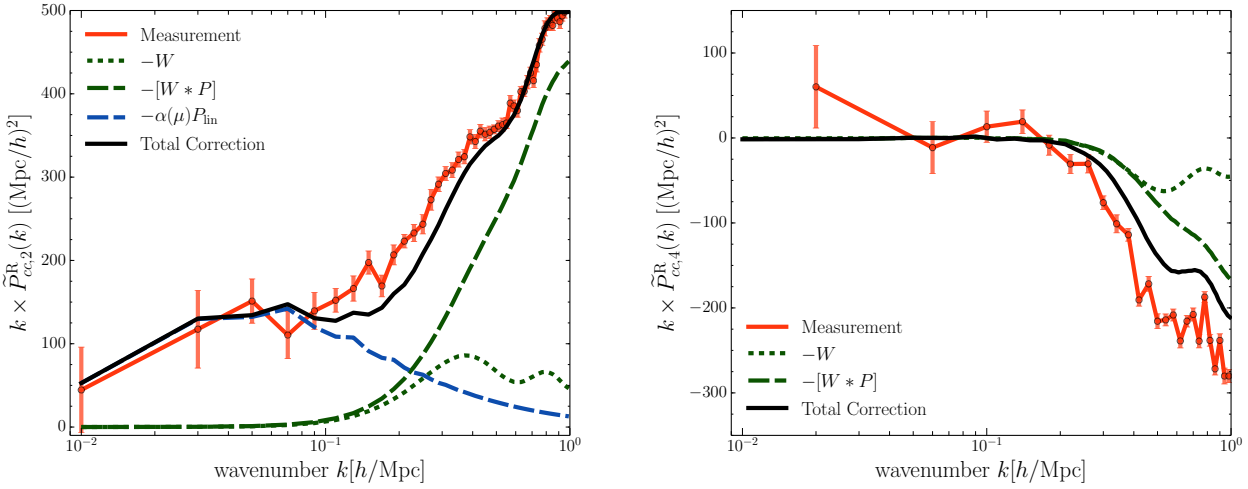


Figure 8. Correction terms of apparent anisotropic clustering of CGM halos; the terms modeling the anisotropic cylinder window and its exclusion effect (the 2nd and 3rd terms on the r.h.s. of equation 13) and the term correcting for the large-scale, anisotropic clustering due to misidentified CGM halos that tend to occur in large-scale structures aligned with the line-of-sight direction (the 4th term in equation 13). The data points with errorbars are the quadrupole (left panel) and hexadecapole (right) power spectra of CGM halos in *real space*, similar to the right panel of Fig. 6, which should vanish if the CGM halo reconstruction is perfect. The dotted and dashed green-curves are the terms involving the cylinder window, multiplied by (-1). The dashed blue curve is the apparent large-scale clustering of misidentified CGM halos, multiplied by (-1). The black curves are the sum of the correction terms, designed to cancel the power spectrum of CGM halos.

In the next subsection, we test how well equation (13) can be used to reproduce the anisotropy introduced even in the real space power spectrum of CGM halos.

5.3 Corrections for the CGM anisotropies and exclusion effects

The two terms in equation (13), which involve the window function W, correct for the apparent anisotropy due to the shape of the cylinder. Since we know the shape of the cylinders to be placed around each galaxy, we can analytically compute the Fourier transform of the window function used in the halo reconstruction (i.e. equation 14).

The left panel of Fig. 8 compares the model prediction of equation (13) with the *real-space* quadrupole power spectrum of CGM central galaxies. The dashed and dotted curves show the quadrupole power spectra arising from the halo exclusion effect via the anisotropic window function:

$$W_2(k) \equiv 5\int_0^1 {\rm d}\mu\, W(\mathbf{k})\mathcal{L}_2(\mu),$$
$$\left[W(\mathbf{k})*\widetilde{P}^R_{\rm cc,0}(k)\right]_2(k) \equiv 5\int_0^1 {\rm d}\mu\, \left[W(\mathbf{k})*\widetilde{P}^R_{\rm cc,0}(k)\right](\mathbf{k})\mathcal{L}_2(\mu), \quad (19)$$

where we have used the monopole power spectrum of CGM halos as $P_{\rm cc}(k)$ to estimate the convolution term. Note that these terms have negative values. The figure shows that the sum of these two terms can explain some fraction of the apparent quadrupole power spectrum (the data points with errorbars), and especially reproduce the qualitative behavior of the quadrupole power; an increasing power with increasing k at $k \gtrsim 0.1\ h\,{\rm Mpc}^{-1}$. However, since the size of a cylinder is a few 10 Mpc$/h$ at most and its window $|W(\mathbf{k})| \to 0$ for small k-limit, the above two terms cannot explain the apparent quadrupole at large length scales, $k \lesssim 0.1\ h\,{\rm Mpc}^{-1}$.

We argue that the small-k apparent anisotropy in the CGM halo clustering can be ascribed to misidentified halos in the CG method. The misidentification tends to occur in an overdensity region that is aligned with the line-of-sight direction, e.g., a filament. Hence as implied from Figs. 6 and 7, the apparent anisotropy at large scales are mainly from cross-correlations of the misidentified CGM satellites in the cosmic web with the CGM central galaxies. We assume that the large-scale apparent anisotropy seen in real space is proportional to the linear matter power spectrum with the anisotropic factor:

$$\Delta P^R(\mathbf{k}) = \alpha(\mu)P^R_{\rm lin}(k), \quad (20)$$

with

$$\alpha(\mu) = \alpha_{\mu^0} - \alpha_{\mu^2}\mu^2, \quad (21)$$

where α_{μ^0} and α_{μ^2} are free parameters. Thus we assume that the apparent anisotropic clustering can be explained by with $O(\mu^2)$ correction term. The monopole and quadrupole power spectra are given by

$$\Delta P^R_0(k) = \left(\alpha_{\mu^0} - \frac{\alpha_{\mu^2}}{3}\right)P^R_{\rm lin}(k), \quad (22)$$
$$\Delta P^R_2(k) = -\frac{2\alpha_{\mu^2}}{3}P^R_{\rm lin}(k)\,. \quad (23)$$

The blue dashed curve in the left panel of Fig. 8 shows the best-fitting model of equation (23), where we have estimated the best-fitting parameter α_{μ^2} by fitting equation (23), multiplied by negative sign (-1), to the quadrupole spectrum of CGM halo power spectrum, over the range $k \in [0.01, 0.05]\ h\,{\rm Mpc}^{-1}$. We obtain $\alpha_{\mu^2} = 0.503$ for our fiducial model. The bold, black curve in the figure shows the total power of the window terms (equation 19) and the correction power spectrum (equation 23) which fairly well reproduces the overall shape of the apparent quadrupole power spec-

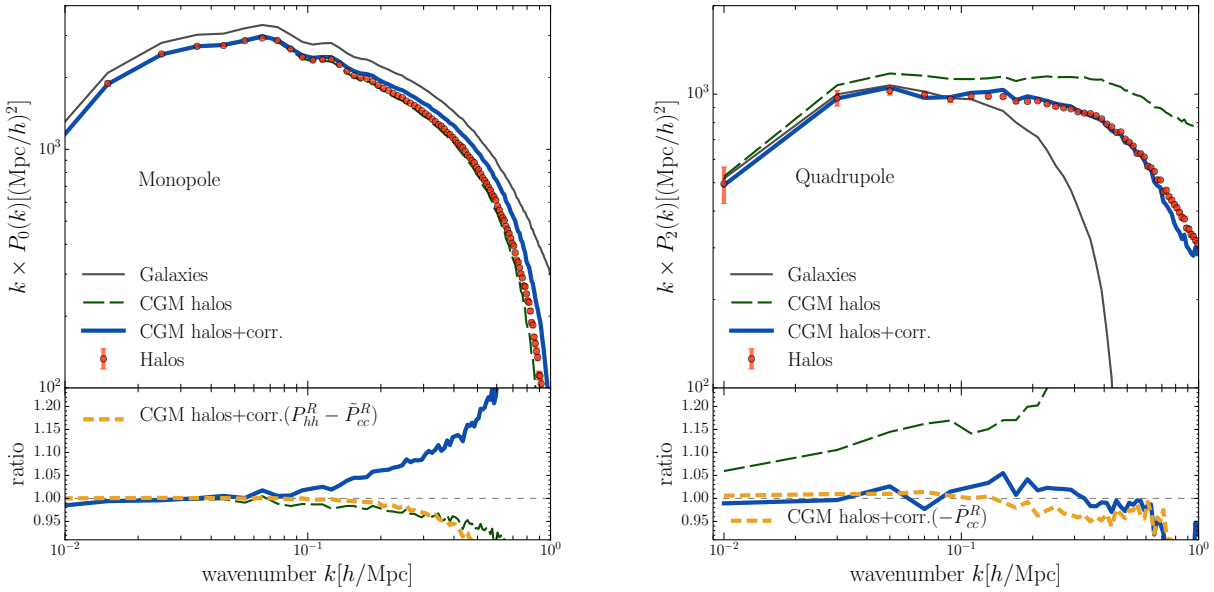


Figure 9. (*Upper panels*) Reconstructed monopole (left) and quadrupole (right) power spectra of halos in redshift space, which are given by a sum of the power spectrum of CGM halos and the correction terms (equation 13). The bold solid curve is the result for our method for the monopole (left panel) and quadrupole (right) spectra, compared with the redshift-space spectra of the underlying true host halos (red points). We assumed the same model in real space, given in Fig. 8, to compute the correction terms, hence did not introduce any additional free parameter to compute the model prediction. For comparison, the thin, green dashed curve shows the results for CGM halos without the correction terms, and the gray solid curves are the spectra of mock galaxies. (*Lower panels*) Ratios of the power spectrum of reconstructed halos to that of true halos. The green and blue curves are for the spectrum without and with the correction, corresponding to the curves with the same color in the upper panels. The yellow, dashed curve is similar to the blue solid line but the result with the large-scale correction term determined by the non-parametric way.

trum of CGM halos, although there is a small but residual systematic offset. Note that the physical RSD effect caused by coherent peculiar motions of halos is much greater than the apparent power that we discussed here, by about factor of 10 (see Fig. 1). The result for a larger cylinder window $(\Delta r_\perp, \Delta r_\parallel) = (1.5, 30)[\,h^{-1}\,\mathrm{Mpc}]$, instead of our fiducial values $(\Delta r_\perp, \Delta r_\parallel) = (1.5, 15)[\,h^{-1}\,\mathrm{Mpc}]$, will be presented in Appendix A and Fig. A2.

The simple form for $\alpha(\mu)$ can be justified using the right hand panel of Fig. 8, which shows the apparent hexadecapole power of the real-space CGM halo spectrum, that arises due to the anisotropic shape of the cylinder. If the correlation of misidentified CGM halos produced anisotropies of order higher than μ^2, it would generate a non-zero hexadecapole on large scales. However, the measured CGM halo hexadecapole is consistent with a null signal at $k < 0.2\,h\,\mathrm{Mpc}^{-1}$. This implies $\Delta P^R_4 = 0$, thus provides a justification of the truncation of the coefficients, $\alpha_{\mu^{2L}} = 0$ $(L \geqslant 2)$. Note that large scatter at different k bins is due to the discrete summation over μ to compute the hexadecapole spectrum for a given Fourier resolution. The black solid curve is the sum of the two window terms multiplied by (-1), and it explains the measured real-space hexadecapole very well.

5.4 Power spectra of CGM halos in redshift space

We now show the main results of this paper; we study how the CGM-constructed halo power spectrum, with the correction terms in equation (13), can reproduce the redshift-space power spectrum of the underlying halos. In this subsection we consider the low-density mock sample, and show the results for the high density sample in Appendix B.

We first discuss the correction terms for the CGM-halo spectrum in redshift space. For the window terms, W and $[W * P]$, we can directly compute the multipole power spectra as presented in Fig. 8. For the apparent anisotropic clustering on large scales, we simply assume that the apparent anisotropy arises from the intrinsic distribution of galaxies in large-scale structure, compared to the CGM technique. That is, we assume that the same correction term (equation 20), derived for the real-space quadrupole spectrum of CGM halos in Fig. 8, can correct for the large-scale apparent clustering even in redshift space:

$$\Delta P^S(\mathbf{k}) \quad \simeq \quad \Delta P^R(\mathbf{k}). \tag{24}$$

This term involves two free parameters for the fiducial cosmological model: α_{μ^0} and α_{μ^2} for the α function. We now estimate the best-fitting α_{μ^0} in a similar manner to our real space analysis such that the model matches the residuals between the real-space monopole power spectra of the true halos and the CGM halos on large scales, $0.01 < k < 0.05\,h\,\mathrm{Mpc}^{-1}$. We obtain the best-fitting parameters $\alpha_{\mu^0} = 0.246$ (and $\alpha_{\mu^2} = 0.503$). Thus, to test our model for the redshift-space halo power spectrum, we do not introduce any additional free parameter.

In Fig. 9, we compare the monopole and quadrupole power spectra of halos in redshift space with the model prediction (equation 13). To compute these redshift-space power spectra, we use the peculiar velocities of halos hosting the CGM central galaxies for simplicity; in other words we ignore possible internal motion of the CGM central galaxy inside the host halo. We will discuss the FoG effect of CGM central galaxies in Appendix C.

Let us first focus on the quadrupole power spectrum (right panel), which is important in order to measure the RSD effect. The upper thin, green dashed curve shows the spectrum for the CGM halos, i.e. the spectrum obtained from a naive implementation of

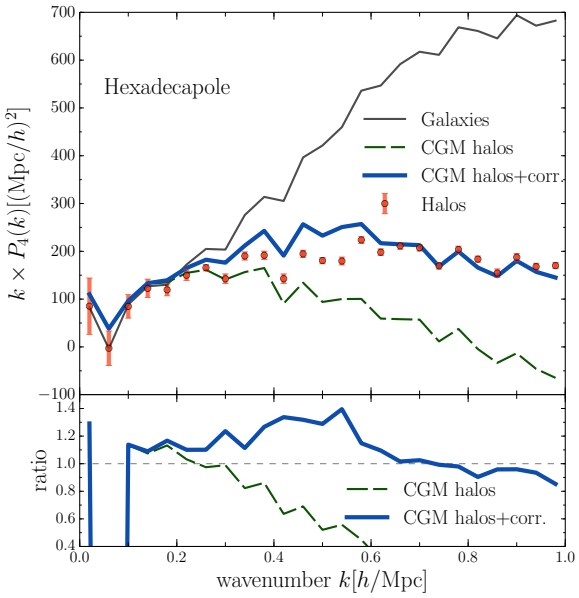


Figure 10. Similar to the previous figure, but for the hexadecapole power spectrum.

the CGM halo reconstruction. This spectrum leads to a systematic overestimation of the underlying halo power spectrum over all the wavenumbers plotted; the deviation is about 15% in power at $k \simeq 0.1\ h\,\mathrm{Mpc}^{-1}$ and becomes $\gtrsim 20\%$ at $k \gtrsim 0.2\ h\,\mathrm{Mpc}^{-1}$, as seen in the bottom panel. On the other hand, the bold blue curve is the result for the quadrupole power spectrum of equation (13) including the CGM window correction (equation 19) and the large-scale correction (equation 24). This is now in excellent agreement with the power spectrum of the underlying halos to within $\sim 5\%$ in the power over all the k range, even up to $k \simeq 0.5\ h\,\mathrm{Mpc}^{-1}$. This implies that the model we develop in this paper can predict the quadrupole power spectrum of CGM selected halos in both real and redshift space simultaneously. This agreement is a huge improvement compared to the quadrupole power spectrum of galaxies.

The upper left panel of Fig. 9 shows similar results for the monopole power spectrum. Our model improves the agreement with the spectrum of halos at small k, once the large scale correction is included. However, the agreement in the weakly nonlinear regime of $k \gtrsim 0.1\ h\,\mathrm{Mpc}^{-1}$ is not as good as that for the quadrupole spectrum. This could be ascribed to a residual shot noise contribution that is caused by the difference between the number densities of the true halos and the CGM halos (see Table 2). The discrepancy at $k > 0.1\,h\,\mathrm{Mpc}^{-1}$ can be further improved by adding an additional free parameter to model the residual shot noise (e.g., Beutler et al. 2014). The ratio of the monopole and quadrupole power spectra at each k bin provides a way to measure the scale-dependent RSD effect: the Kaiser factor in the linear regime of $k \lesssim 0.1\ h\,\mathrm{Mpc}^{-1}$ and the nonlinear RSD effect at the larger k bins. These signals are direct predictions of the ΛCDM structure formation model, and can be used to test theory of gravity at the respective scales. The results in Fig. 9 show that our model should enable us to measure the RSD effect to within 5% accuracy for scales up to $k \sim$ a few $0.1\ h\,\mathrm{Mpc}^{-1}$, and also the assumption that the large-scale correction to the power spectrum in redshift space is the same as that in real space (equation 24) is reasonable.

We further examine the hexadecapole power spectrum in Fig. 10. The hexadecapole spectrum has a smaller power than the quadrupole for the ΛCDM model as predicted by the Kaiser formula. However, the nonlinear RSD effect can to some extent enhance the power (Scoccimarro 2004; Taruya et al. 2010). In addition, the FoG effect causes a significant power in the hexadecapole spectrum as shown by the upper solid curve (also see Hikage & Yamamoto 2013). Hence, the hexadecapole spectrum at least gives a useful consistency check of the measurement and/or the systematic effects. The figure shows that our model including the correction terms nicely reproduces the results from the mock catalog, over the range of k we consider. As is the case for the real-space hexadecapole, implementing the CG technique does not produce the apparent anisotropy in the redshift-space hexadecapole at $k < 0.2\ h^{-1}\,\mathrm{Mpc}$. It thus implies $\Delta P_4^S = \Delta P_4^R = 0$ and provides another justification of the ansatz we used in equation (24).

In the above analysis we have determined the large-scale corrections by parameterizing $\alpha(\mu)$ using equation (21). For the quadrupole, we have used the black line in the left panel of Fig. 8 as the total correction to the CGM halo spectrum. Now, we present an alternative non-parametric way to correct the CGM halo spectrum. We use the difference between the observed monopole and quadrupole of the real space CGM halo power spectrum to those of the underlying halo power spectrum as a correction for the monopole and quadrupole of the CGM halo power spectrum in redshift space. This corresponds to using the red points for the quadrupole correction. The procedure corresponds to the following model:

$$P^S_{\mathrm{hh},0}(k) \simeq \widetilde{P}^S_{\mathrm{cc},0}(k) + P^R_{\mathrm{hh},0}(k) - \widetilde{P}^R_{\mathrm{cc},0}(k), \quad (25)$$

$$P^S_{\mathrm{hh},2}(k) \simeq \widetilde{P}^S_{\mathrm{cc},2}(k) - \widetilde{P}^R_{\mathrm{cc},2}(k). \quad (26)$$

The results of using such a non-parametric correction for the monopole and quadrupole spectra are shown using the yellow dashed lines in the lower left and right panels of Fig. 9, respectively. While there is a slight improvement for the monopole compared to the parametric case presented by the blue solid line, the accuracy for the quadrupole is similar to the one in the parametric case. The agreement confirms that the large-scale apparent anisotropic clustering arises mainly from the intrinsic distribution of galaxies.

Note that the correction term for the large-scale anisotropy is modeled using the real-space multipole power spectra (equation 24), which are not an observable in real galaxy surveys. Although the contribution of the large-scale anisotropy from the misidentified halos is only about 15% and 20% of the RSD quadrupole at $k = 0.15\,h\,\mathrm{Mpc}^{-1}$ and $0.2\,h\,\mathrm{Mpc}^{-1}$, respectively, the cosmological information would be reduced if the corrections parameters α_{μ^0} and α_{μ^2} were treated as free parameters and marginalized over. Instead, we propose to use the mock catalog in order to derive priors on the correction $\alpha(\mu)$ in real galaxy surveys (see Fig. 8). This procedure will be tested in detail and applied to the real data in our future work.

Note also that the accuracy of our model to reconstruct the halo power spectrum depends on the choice of the cylinder size, particular its height, $\Delta r_\parallel$. The size needs to be determined by taking into account the number density of the given galaxy sample as well as properties of the galaxies. In order to see the sensitivity of the choice of $\Delta r_\parallel$ on the final result, we repeated the same analysis by adopting the size much larger than the RSD displacement scale, $\Delta r_\parallel = 30\ h^{-1}\,\mathrm{Mpc}$ in Appendix A. By comparing the right panel of Fig. 9 and Fig. A3, one can see that the accuracy of our model is

not very sensitive to the choice of the cylinder size. Nevertheless, we will use mock catalogs to calibrate the appropriate cylinder size when we analyze the real data.

6 DISCUSSION AND CONCLUSION

In this paper we have developed a novel method for reconstructing the power spectrum of dark matter halos from the observed galaxy distribution in redshift space. The central tenet of our method is that satellite galaxies are a nuisance to infer cosmological parameters from galaxy clustering. Therefore, we remove satellite galaxies from the sample used to measure the anisotropic clustering of galaxies. This minimizes the 1-halo term contribution as well as the Finger-of-God (FoG) effect due to virial motions of satellite galaxies in massive halos, and makes the measured clustering signal more sensitive to the typical halos hosting the central galaxies of the sample.

Our method relies on the cylinder-grouping (CG) method, which sorts galaxies in a given catalog in descending order of their luminosity or stellar masses, places a cylinder around each galaxy from the top of the sorted list and regards all the galaxies inside the cylinder as member galaxies of a halo. This is similar but simpler than the redshift space FOF method used by Reid & Spergel (2009). Since the line-of-sight length of cylinder has to be long enough to cover a possible large displacement due to the virial motions of galaxies, our fiducial choice of $\Delta r_{\parallel} = 15\ h^{-1}\ \mathrm{Mpc}$ seems sufficient to remove most of the satellite galaxies around massive halos. However, we found that our method generates an apparent anisotropy in the distribution of CGM-selected halos due to the anisotropy of the cylinder used to identify satellite galaxies. We showed that this apparent anisotropy can be corrected for (equation 13), using the cylindrical window function on small scales as well as the linear matter power spectrum with coefficients up to the order μ^2 on large scales.

We tested the accuracy of our method using mock galaxy catalogs at $z = 0.5$, which are constructed from N-body simulations to mimic the SDSS-III BOSS survey. We first studied the quadrupole power spectrum of CGM halos in *real space*, which is caused by the apparent anisotropic clustering that we discussed above. We showed that the correction terms involving the cylindrical window can explain most of the quadrupole power at $k \gtrsim 0.1\ \ h\,\mathrm{Mpc}^{-1}$. On the other hand, the apparent clustering at smaller k can be explained by our model, by adjusting the model parameter (α_{μ^2} for the quadrupole power spectrum), as shown in Figs. 8. The sum of these correction terms can fairly well reproduce the apparent quadrupole power. Next, we showed that our model can also reproduce the redshift-space quadrupole power spectrum of the underlying halos, to an accuracy to within 5% in the power up to $k \simeq 0.5\,h\,\mathrm{Mpc}^{-1}$. To arrive at this result, we did not introduce any additional parameter: we assumed that the large-scale apparent clustering is given by the above correction function in real space. Even if we allow model parameters (α_{μ^0} and α_{μ^2}) to freely vary, we found a similar-level agreement. The correction term is about 10% in the quadrupole power at $k \sim 0.1\ \ h\,\mathrm{Mpc}^{-1}$, while the correction terms involving the cylindrical window give about 40% at $k \sim 0.5\ \ h\,\mathrm{Mpc}^{-1}$, for a galaxy mock catalog (with number density of $\bar{n}_g \sim 10^{-4}\ (\,h\,\mathrm{Mpc}^{-1})^3$, similar to LRGs or massive CMASS galaxies). If we use a galaxy sample with a higher number density, the contributions of the correction terms are greater.

The agreement of our model with the underlying halo power spectrum is encouraging. If we can use the measured quadrupole spectrum up to the weakly nonlinear regime $k \gtrsim 0.1\,h\,\mathrm{Mpc}^{-1}$, it promises a significant improvement in the RSD measurement: e.g., the clustering information up to maximum wavenumber $k = 0.2\,h\,\mathrm{Mpc}^{-1}$ is equivalent to a galaxy survey with about factor of 8 wider area using the information up to $k = 0.1\,h\,\mathrm{Mpc}^{-1}$. However, in the weakly nonlinear regime the Kaiser factor is no longer valid, and the RSD effect becomes scale-dependent due to nonlinear mode coupling (Scoccimarro 2004). Nevertheless, the halo power spectrum, if recovered, enables a direct comparison with model halo power spectrum estimated from a suite of N-body simulations. For the cosmological analysis, we need to construct a "cosmic emulator" of redshift-space power spectra of halos given as a function of halo mass, redshift and cosmological models (Nishimichi et al. in preparation). If the satellite galaxy contribution can be shown to be negligible and robust to a variety of methods that populate satellite galaxies in halos, one could even build emulator of redshift space power spectra of halos, where these halos are filtered using cylinders of the same size as used in data, allowing a direct comparison to observations (and bypassing the need for an accurate empirical model as constructed in this paper). The ratio of the monopole and quadrupole spectra of halos contains a wealth of information about the RSD effect, thereby allowing us to improve the constraints on the growth of large-scale structure. In addition, the scale-dependent RSD effects can be used to test theories of gravity on these scales. We will explore these avenues in future work.

The inability of redshift surveys to obtain redshifts of closely spaced galaxies due to fiber collisions is one of the biggest hindrance to use RSDs for precision cosmology (Lin et al. 1996; Reid et al. 2014). Fiber collisions become more important for future high-z surveys because a fixed angular scale corresponds to a larger scale at higher redshifts. Since our CGM halo reconstruction method needs to keep only one galaxy out of the host halo, our model is less affected by fiber collisions.

There are several effects that we ignored in this paper that should be taken into account for an implementation of this method for real data. We have not discussed the mis-centering of (brightest or most massive) galaxies in their halos (Hikage et al. 2013) (see also Skibba et al. 2011; Hikage et al. 2012; Masaki et al. 2013; Hoshino et al. 2015; Saito et al. 2016). This becomes especially true if the spectroscopic target galaxies are selected based on cuts in magnitude and color space from the imaging data. This is indeed the case for all spectroscopic surveys, and the true central galaxies may not necessarily make the targeting cut. The off-centered galaxies can in principle be constrained by combining the redshift-space clustering of CGM halos with the weak gravitational lensing signal (or cross-correlation with photometric galaxies). Gravitational lensing can probe the matter distribution around the true center, as proposed in Hikage et al. (2012) (also see Oguri & Takada 2011; Hikage et al. 2013).

The next logical step is to apply this method to existing data from galaxy surveys, such as the CMASS sample of BOSS survey. In order to stress our method, we need to use a more accurate mock catalog of the CMASS sample to calibrate possible residual systematic errors. The mock catalog can be used to add theory priors on model parameters in our method (the coefficient parameters to model the large-scale apparent clustering). In particular, the footprint of the ongoing Subaru Hyper Suprime-Cam (HSC) survey (Miyazaki et al. 2012) fully overlaps with the BOSS survey. This will allow us to combine the redshift-space power spectrum of CGM halos, reconstructed from the CMASS galaxies, with the galaxy-galaxy weak lensing, as we discussed above. Ultimately, our

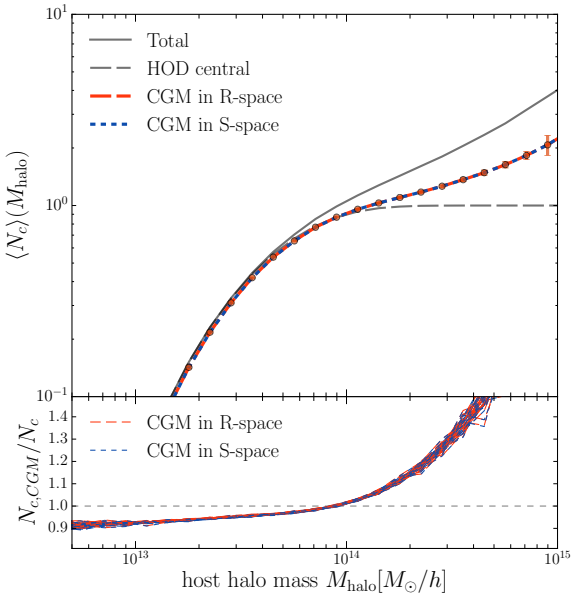


Figure A1. Same as Fig.5 but with the cylinder size $(\Delta r_\perp, \Delta r_\parallel) = (1.5, 30)\ h^{-1}$ Mpc.

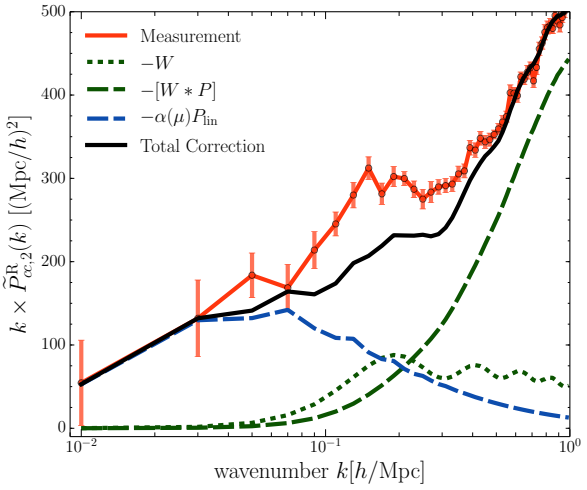


Figure A2. Same as Fig. 8 but for the different cylinder size, $\Delta r_\parallel = 30\ h^{-1}$ Mpc.

goal is to apply our method to even larger, higher-redshift galaxy surveys such as the Subaru Prime Focus Spectrograph (PFS) survey (Takada et al. 2014). Since the PFS combined with HSC promises to provide very tight constraints on cosmological models, we need to carefully test whether the accuracy we have obtained in this paper for the theoretical modeling scheme is sufficient given the statistical power of these surveys. This will be addressed in future work.

ACKNOWLEDGMENTS

We thank Beth Reid and Uroš Seljak for useful discussion at the early stage of this work. T.O. is supported by JSPS KAKENHI Grant Number JP26887012. This work is in part supported by Grant-in-Aid for Scientific Research from the JSPS Promotion of Science (No. 23340061 and 26610058), MEXT Grant-in-Aid for Scientific Research on Innovative Areas (No. 15H05893, 15K21733, 15H05892) and JSPS Program for Advancing Strategic International Networks to Accelerate the Circulation of Talented Researchers.

APPENDIX A: CHANGING THE CYLINDER SIZE

The size of the cylinder, namely the radius ($\Delta r_\perp$) and height ($2\Delta r_\parallel$), is arbitrary, and depends upon the galaxy sample being considered. These should be chosen so that the majority of the multiple systems are properly classified as centrals and satellites but to be as small as possible in order to avoid larger corrections. Especially, the choice of $\Delta r_\parallel$ is crucially important since this value determines how well we can eliminate the FoG contamination. Our default values, $(\Delta r_\perp, \Delta r_\parallel) = (1.5, 15)[\ h^{-1}$ Mpc], are such an optimal choice. On the other hand, a galaxy pair in the same halo but separated along the transverse direction has a small FoG effect, and so imperfect grouping for such satellites does not affect the measurements by a large amount.

Fig. 4 implies that there exist galaxy pairs in the same massive halo are not identified due to a small $\Delta r_\perp$, rather than $\Delta r_\parallel$. Thus the failure of identifying the members of the massive halos seen in Fig.5 is not expected to cause a serious problem. In order to explore the effects of a larger cylinder in the redshift direction, we adopt a cylinder height $\Delta r_\parallel = 30\ h^{-1}$ Mpc, and repeat the same analysis for the low-density galaxy sample. Fig. A1 is the same as Fig. 5 but with $\Delta r_\parallel = 30\ h^{-1}$ Mpc. There is almost no difference between the two cases, implying that $\Delta r_\parallel = 15\ h^{-1}$ Mpc is large enough to identify the galaxies with the radial displacements by the FoG and the the behavior of $N_{\rm c,CGM}/N_{\rm c} > 1$ for large $M_{\rm halo}$ is due to the galaxy pairs along the tangential direction.

Fig. A2 plots the real-space quadrupole power spectrum, the same as Fig. 8 but with $\Delta r_\parallel = 30\ h^{-1}$ Mpc. Due to the larger cylinder height, the exclusion effect is more significant. Just like Fig. 8, the sum of the window function W and its convolution $[W * \widetilde{P}]$ as depicted by the solid black line captures the measured real-space quadrupole while there is a systematic offset at $k > 0.1\ h\ {\rm Mpc}^{-1}$. The final result of our correction model for the redshift-space quadrupole is shown in Fig. A3. As seen in the bottom panel, our model presented by the solid blue line achieves the accuracy of better than 5-7% on scales $k < 1\ h\ {\rm Mpc}^{-1}$ although we adopt such an extremely large cylinder size. Furthermore, the model with the correction terms directly determined from the real-space measurement, shown as the yellow dashed line, has almost the same accuracy as the result with $\Delta r_\parallel = 15\ h^{-1}$ Mpc.

APPENDIX B: RESULTS FOR HIGH-DENSITY SAMPLE

The performance of our correction model depends on the number density of the galaxy sample. As we have seen in Section 5.1, larger corrections are required for a higher-density sample. In this appendix we present the results when we apply the same technique to the high-density mock sample with $\bar{n} = 3.4 \times 10^{-4}(\ h\ {\rm Mpc}^{-1})^3$, roughly corresponding to the full BOSS CMASS galaxy sample without any stellar mass cut.

The results for the high-density sample are shown for the

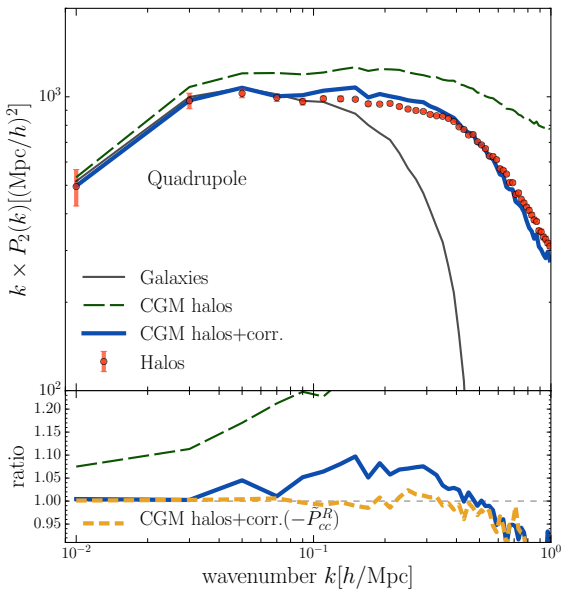


Figure A3. Same as Fig. 9 but for the different cylinder size, $\Delta r_{\parallel} = 30\,h^{-1}$ Mpc.

monopole (left) and quadrupole (right) spectra in Fig. B1. For the monopole, the CGM halo spectrum without the correction terms has $> 5\%$ offset from the true halo spectrum even on large scales. However, this can be corrected for by our model to within 5% accuracy up to $k \sim 0.3\,h\,\mathrm{Mpc}^{-1}$ as shown in the bottom left panel. The coefficients of equations (22) and (23) for the high-density sample are, $\alpha_{\mu^0} = 0.399$ and $\alpha_{\mu^2} = 0.594$. For the quadrupole, there is $\sim 20\%$ offset of the CGM halo spectrum without correction from the true halo spectrum at $k < 0.1\,h\,\mathrm{Mpc}^{-1}$ and it blows up to 30% at $k \sim 0.2\,h\,\mathrm{Mpc}^{-1}$. Our correction model can improve the results to a large extent, but a discrepancy of $\sim 10\%$ remains if we adopt the non-parametric model for the large-scale correction, as shown by the gray dashed line at the right bottom panel of Fig. B1. In comparison to Fig. 9, one can see that the accuracy of our correction model certainly depends on the number density of the sample and the lower-density sample gives more precise results as expected.

APPENDIX C: EFFECT OF OFF-CENTERED GALAXIES

The main results presented in Fig. 9 assumed that the off-centering effect of central galaxies can be perfectly corrected for using the galaxy-galaxy lensing. In this appendix we focus on the situation that we analyze only the galaxy clustering data, i.e., without any knowledge or constraints on the off-centering effect.

The results for the monopole and quadrupole without correction for the off-centering effect are shown in the top panels of Fig. C1. The thin gray lines are the original galaxy power spectra, the same as those presented in Fig. 9. The red points are the power spectrum of halos, but to make a fair comparison, this power spectrum includes the residual FoG effect due to miscentering unlike that in Fig. C1. Thus it is equivalent to the power spectrum of central galaxies $P^S_{\rm cc}$, a small fraction of which are actually not at the center of the halos. The green dashed lines are the multipoles of the CGM halos, which are slightly suppressed at small scales relative to the thin lines in Fig. C1 due to the residual FoG effect. Thus, the reconstructed halo power spectra are suppressed by a similar amount, as shown as the thick dashed lines. Here the large-scale correction $\alpha(\mu)P^R_{\rm lin}(k)$ is the same and only the differences arise from the CGM window and its convolution with the underlying power spectrum.

The bottom panels of Fig. C1 show the ratios of the reconstructed spectra of halos to those of central galaxies. The denominators include the FoG from off-centered galaxies, while the numerators have both the FoG effect as well as the residual FoG from the satellites which were failed to captured by the CGM. Thus the ratios are suppressed relative to the case where the FoG effect is assumed to be perfectly corrected for using galaxy-galaxy lensing as shown at the bottom panels of Fig. 9. Even though we do not correct for the FoG, a similar precision can obtained for the halo power spectrum reconstruction.

APPENDIX D: VELOCITY BIAS ARISING FROM NONLINEAR TRANSFORMATION

Seljak (2012) showed that any nonlinear transformation of data in redshift space would create velocity bias. This is exactly the case for our model prescription since placing cylinders on redshift-space galaxy distribution to identify CGM halos is also a nonlinear transformation, $\delta^S_{\rm g} \to \widetilde{\delta}^S_{\rm h} = F(\delta^S_{\rm g})$. To see if the CG method produces the velocity bias, we consider to modify Eq. (13) and repeat the analysis as follows. First, the cylinders are placed at the positions of galaxies in redshift space. We then measure $\widetilde{P}^S_{cc}$ and replace the convolution term in equation (11) by $\left[W(\mathbf{k}) * \widetilde{P}^S_{cc,0}(k)\right]$. We determine the large-scale coefficient parameters α_{μ^0} and α_{μ^2} by comparing with the real-space multipoles of the CGM halos (note again that the cylinders are identified in redshift space). The determined coefficients are used to model the reconstructed halo power spectrum in redshift space. In this way, the reconstructed spectrum would inevitably contain the velocity bias according to Seljak (2012), and the modeling result would be biased compared to the result shown in Section 5.4.

The coefficients are determined to exactly the same values as our default case, $\alpha_{\mu^0} = 0.246$ and $\alpha_{\mu^2} = 0.503$. We find that the accuracy of the reconstructed quadrupole spectrum of halos is within 6%, almost the same as the accuracy of 5% for the default case. We thus conclude that the velocity bias arising from the CG method is negligibly small. However, we will investigate this effect in more detail in our future work.

REFERENCES

Baldauf T., Seljak U., Smith R. E., Hamaus N., Desjacques V., 2013, Phys. Rev. D, 88, 083507
Baldauf T., Codis S., Desjacques V., Pichon C., 2016, MNRAS, 456, 3985
Behroozi P. S., Wechsler R. H., Wu H.-Y., 2013, ApJ, 762, 109
Berlind A. A., et al., 2006, ApJS, 167, 1
Bernardeau F., Colombi S., Gaztañaga E., Scoccimarro R., 2002, Phys. Rep., 367, 1
Beutler F., et al., 2014, MNRAS, 443, 1065
Bryan G. L., Norman M. L., 1998, ApJ, 495, 80
Cole S., Fisher K. B., Weinberg D. H., 1994, MNRAS, 267, 785
Cooray A., Sheth R., 2002, Phys. Rep., 372, 1
Davis M., Efstathiou G., Frenk C. S., White S. D. M., 1985, ApJ, 292, 371
Eisenstein D. J., et al., 2005, ApJ, 633, 560
Eisenstein D. J., et al., 2011, AJ, 142, 72
Hamilton A. J. S., 1992, ApJ, 385, L5

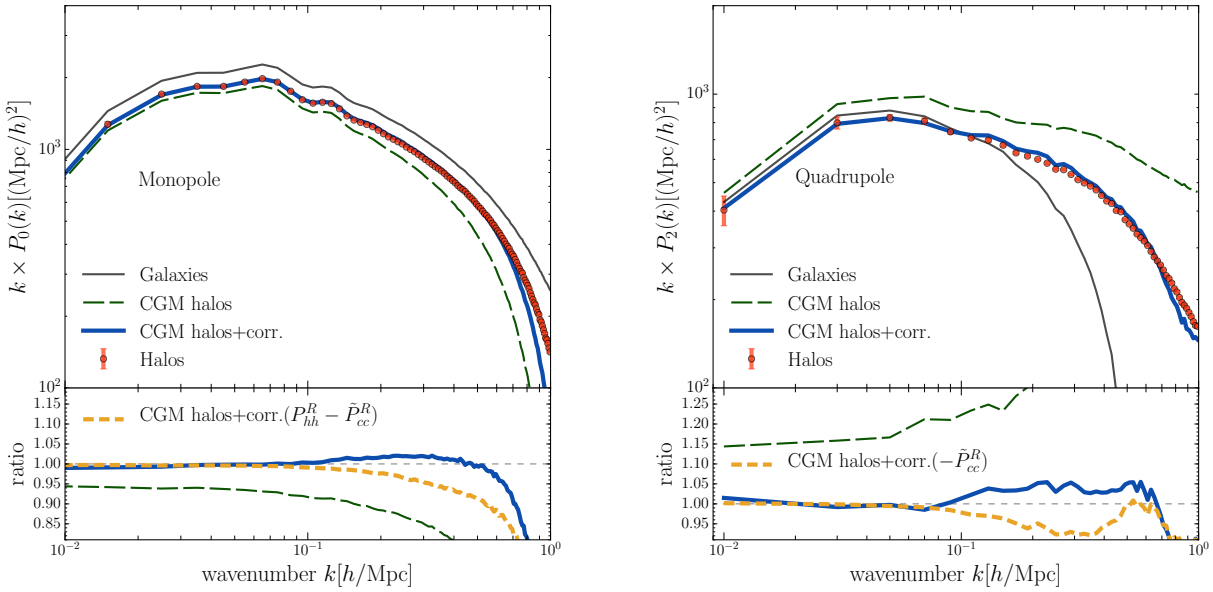


Figure B1. Same as 9, but for the higher density sample.

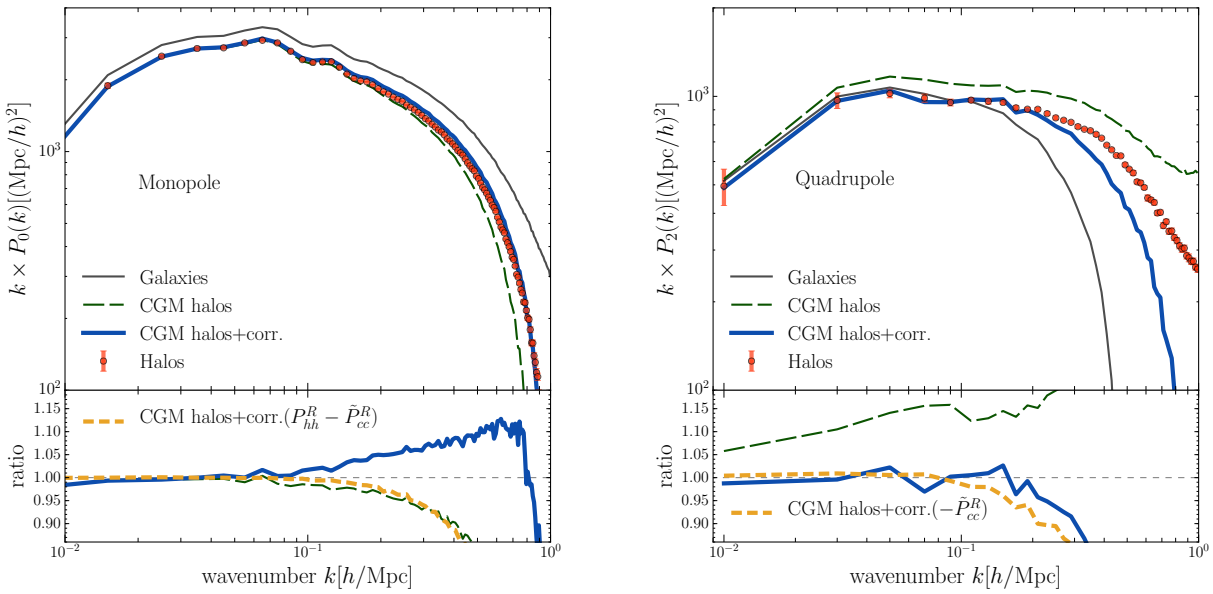


Figure C1. Same as Fig. 9 but the off-centering effect of central galaxies are not corrected and the results compared to the results of central galaxies. As a fair comparison, the red points at the top panels here include the residual FoG effect from the central galaxies which have offset.

Hamilton A. J. S., 1998, in D. Hamilton ed., Astrophysics and Space Science Library Vol. 231, The Evolving Universe. pp 185–+ (arXiv:astro-ph/9708102)

Hikage C., Yamamoto K., 2013, J. Cosmology Astropart. Phys., 8, 19

Hikage C., Takada M., Spergel D. N., 2012, MNRAS, 419, 3457

Hikage C., Mandelbaum R., Takada M., Spergel D. N., 2013, MNRAS, 435, 2345

Hoshino H., et al., 2015, MNRAS, 452, 998

Jackson J. C., 1972, MNRAS, 156, 1P

Jennings E., Baugh C. M., Pascoli S., 2011, MNRAS, 410, 2081

Jing Y. P., 2005, ApJ, 620, 559

Kaiser N., 1987, MNRAS, 227, 1

Komatsu E., et al., 2009, ApJS, 180, 330

Lewis A., Challinor A., Lasenby A., 2000, ApJ, 538, 473

Lin H., Kirshner R. P., Shectman S. A., Landy S. D., Oemler A., Tucker D. L., Schechter P. L., 1996, ApJ, 471, 617

Masaki S., Hikage C., Takada M., Spergel D. N., Sugiyama N., 2013, MNRAS, 433, 3506

Matsubara T., 2008, Phys. Rev. D, 78, 083519

Miyazaki S., et al., 2012, in Ground-based and Airborne Instrumentation for Astronomy IV. p. 84460Z, doi:10.1117/12.926844

Mohammed I., Seljak U., 2014, MNRAS, 445, 3382

More S., Miyatake H., Mandelbaum R., Takada M., Spergel D. N., Brownstein J. R., Schneider D. P., 2015, ApJ, 806, 2

Nishimichi T., Taruya A., 2011, Phys. Rev. D, 84, 043526

Nishizawa A. J., Takada M., Nishimichi T., 2013, MNRAS, 433, 209

Oguri M., Takada M., 2011, Phys. Rev. D, 83, 023008
Okumura T., Jing Y. P., 2011, ApJ, 726, 5
Okumura T., Seljak U., McDonald P., Desjacques V., 2012a, J. Cosmology Astropart. Phys., 2, 10
Okumura T., Seljak U., Desjacques V., 2012b, J. Cosmology Astropart. Phys., 11, 14
Okumura T., Hand N., Seljak U., Vlah Z., Desjacques V., 2015, Phys. Rev. D, 92, 103516
Peacock J. A., Dodds S. J., 1994, MNRAS, 267, 1020
Peebles P. J. E., 1980, The large-scale structure of the universe. Princeton, N.J., Princeton Univ. Press
Reid B. A., Spergel D. N., 2009, ApJ, 698, 143
Reid B. A., White M., 2011, MNRAS, 417, 1913
Reid B. A., et al., 2010, MNRAS, 404, 60
Reid B. A., Seo H.-J., Leauthaud A., Tinker J. L., White M., 2014, MNRAS, 444, 476
Saito S., Baldauf T., Vlah Z., Seljak U., Okumura T., McDonald P., 2014, Phys. Rev. D, 90, 123522
Saito S., et al., 2016, MNRAS, 460, 1457
Sato M., Matsubara T., 2011, Phys. Rev. D, 84, 043501
Scoccimarro R., 2004, Phys. Rev. D, 70, 083007
Seljak U., 2000, MNRAS, 318, 203
Seljak U., 2001, MNRAS, 325, 1359
Seljak U., 2012, J. Cosmology Astropart. Phys., 3, 004
Seljak U., Vlah Z., 2015, Phys. Rev. D, 91, 123516
Seljak U., Zaldarriaga M., 1996, ApJ, 469, 437
Simpson F., Heavens A. F., Heymans C., 2013, Phys. Rev. D, 88, 083510
Skibba R. A., van den Bosch F. C., Yang X., More S., Mo H., Fontanot F., 2011, MNRAS, 410, 417
Smith R. E., Scoccimarro R., Sheth R. K., 2007, Phys. Rev. D, 75, 063512
Springel V., White S. D. M., Tormen G., Kauffmann G., 2001, MNRAS, 328, 726
Takada M., et al., 2014, PASJ, 66, 1
Taruya A., Nishimichi T., Saito S., 2010, Phys. Rev. D, 82, 063522
Tegmark M., et al., 2006, Phys. Rev. D, 74, 123507
Tinker J. L., Weinberg D. H., Zheng Z., 2006, MNRAS, 368, 85
Vlah Z., Seljak U., Okumura T., Desjacques V., 2013, J. Cosmology Astropart. Phys., 10, 53
Weinberg D. H., Mortonson M. J., Eisenstein D. J., Hirata C., Riess A. G., Rozo E., 2013, Phys. Rep., 530, 87
White M., 2001, MNRAS, 321, 1
White M., et al., 2011, ApJ, 728, 126
Zheng Y., Song Y.-S., 2016, J. Cosmology Astropart. Phys., 8, 050
Zheng Z., et al., 2005, ApJ, 633, 791
van den Bosch F. C., More S., Cacciato M., Mo H., Yang X., 2013, MNRAS, 430, 725